High-speed low-light in vivo two-photon voltage imaging of large neuronal populations

Jelena Platisa[1,2,9], **Xin Ye**[3,4,9], **Allison M. Ahrens**[5], **Chang Liu**[3], **Ichun Anderson Chen**[4], **Ian G. Davison**[4,5,6], **Lei Tian**[3,4,7], **Vincent A. Pieribone**[1,2,8,✉], **Jerry L. Chen**[3,4,5,6,✉]

[1]Department of Cellular and Molecular Physiology, Yale University, New Haven, CT, USA.

[2]The John B. Pierce Laboratory, New Haven, CT, USA.

[3]Department of Biomedical Engineering, Boston University, Boston, MA, USA.

[4]Neurophotonics Center, Boston University, Boston, MA, USA.

[5]Department of Biology, Boston University, Boston, MA, USA.

[6]Center for Systems Neuroscience, Boston University, Boston, MA, USA.

[7]Department of Electrical and Computer Engineering, Boston University, Boston, MA, USA.

[8]Department of Neuroscience, Yale University, New Haven, CT, USA.

[9]These authors contributed equally: Jelena Platisa, Xin Ye.

Abstract

Monitoring spiking activity across large neuronal populations at behaviorally relevant timescales is critical for understanding neural circuit function. Unlike calcium imaging, voltage imaging requires kilohertz sampling rates that reduce fluorescence detection to near shot-noise levels. High-photon flux excitation can overcome photon-limited shot noise, but photobleaching and photodamage restrict the number and duration of simultaneously imaged neurons. We investigated an alternative approach aimed at low two-photon flux, which is voltage imaging below the shot-noise limit. This framework involved developing positive-going voltage indicators with improved

spike detection (SpikeyGi and SpikeyGi2); a two-photon microscope ('SMURF') for kilohertz frame rate imaging across a 0.4 mm × 0.4 mm field of view; and a self-supervised denoising algorithm (DeepVID) for inferring fluorescence from shot-noise-limited signals. Through these combined advances, we achieved simultaneous high-speed deep-tissue imaging of more than 100 densely labeled neurons over 1 hour in awake behaving mice. This demonstrates a scalable approach for voltage imaging across increasing neuronal populations.

To understand the nervous system, neuron population activity recordings must span multiple timescales during behavior. Current approaches to image activity at cellular resolution occupy two ends of a spectrum. Large population recordings using calcium imaging occur at slow sampling rates (<15 Hz) and is a poor proxy for action potential activity[1]. To measure spiking accurately using voltage imaging, sampling must be at least an order of magnitude faster (~400 Hz)[2,3]. So far, fast voltage imaging (1 kHz) has only been achieved simultaneously in a small number (~10) of neurons[4–7]. Here, we sought to increase the capacity for high-speed in vivo voltage imaging.

Shot noise and photodamage are two fundamental limits for optically resolving individual action potentials in neuronal populations. Assuming adequate indicator sensitivity, sufficient genetically encoded voltage indicator (GEVI) molecules need to be excited for action-potential-dependent changes in fluorescence to be reliably detected above shot noise. To achieve an adequate signal-to-noise ratio (SNR), current approaches for one-photon and two-photon voltage imaging have relied on 'high-photon flux' regimes in which excitation light is concentrated on only tens of neurons[5,8]. One-photon cellular resolution voltage imaging is achievable using widefield illumination and high-speed cameras, but light scatter limits depth penetration[4,7]. Alternatively, two-photon microscopy enables deeper kilohertz imaging of densely labeled tissue but is restricted to small fields of view (FOVs) because of existing excitation strategies[5,6,9].

Existing two-photon-compatible GEVIs fluoresce at resting membrane potential and decrease their fluorescence during action potentials (that is, they are 'negative-going' indicators)[5,10,11]. For accurate spike detection, high-photon flux is needed to overcome light scatter from this resting state fluorescence that additionally consists of potentially mislocalized GEVI molecules[7,12]. High flux in one photon and two photon induces rapid photobleaching, limiting recording times to several minutes[5,7,12], and cannot be scaled for larger neuronal populations because increasing excitation introduces photodamage[13]. To maintain high speeds, the overall photon budget demands that the amount of excitation per neuron decreases as the neuronal number increases.

Therefore, we took a multidisciplinary approach integrating protein engineering, optical engineering and deep learning to overcome fundamental limits enabling fast voltage imaging across large neuronal populations. We developed a high-speed, positive-going two-photon GEVI; a kilohertz-scanning, large-FOV 'SMURF' (spatiotemporal multiplexed ultrafast resonance frame-scanning) two-photon microscope; and a deep convolutional neural network (DeepVID) for image denoising. Through this synergistic combination of technologies, we provide a framework for population-level two-photon voltage imaging in the awake behaving animal.

Results

Development of positive-going two-photon-compatible GEVI

We previously demonstrated that GEVI signal polarity can be manipulated by modifying the chromophore protonation state, converting the 'negative-going' ArcLight[11] into a 'positive-going' Marina[14] (Fig. 1a). Using a similar approach, we performed directed evolution of the negative-going, two-photon-compatible GEVIs ASAP2f and ASAP3 (refs. [5,10]). Initially, site-directed mutagenesis of amino acid residue H150 within the ASAP2f fluorescent protein resulted in several mutants showing an increase in fluorescence on depolarization. We then used degenerative codons NNKNNK to create an insertion library targeted between residues D151 and N152 in ASAP3 (Fig. 1a,b). Using field stimulation, we screened 1,104 mutants and identified approximately 150 positive-going variants (Fig. 1c). The most sensitive mutant, named SpikeyGi (with sequence D151 D152 S153 N154), had a response of approximately 30% voltage-dependent change in fluorescence divided by the resting fluorescence ($\Delta F/F_0$). We next targeted residues in the linker region between the voltage-sensing domain and fluorescent protein (R149, G150 and D151) and within the fluorescent protein (N167, F168 and V170). Functional screening identified another variant, named SpikeyGi2, containing an isoleucine mutant, V170I, with a response of approximately 75% $\Delta F/F_0$.

We used one-photon imaging (500–1,000 Hz) and whole-cell patch-clamp electrophysiology in HEK293 cells to compare SpikeyGi and SpikeyGi2 with ASAP3 (Fig. 1d,e). SpikeyGi2 showed increased sensitivity to transient 100-mV step depolarizations compared with ASAP3 and SpikeyGi ($\Delta F/F_0$ for SpikeyGi2, $57.5 \pm 3.3\%$, mean ± s.e.m., $n = 6$ cells; $\Delta F/F_0$ for SpikeyGi, $18.7 \pm 1.1\%$, $n = 8$ cells; $\Delta F/F_0$ for ASAP3, $-38.1 \pm 1.6\%$, $n = 8$ cells, Student's t-test; $P = 7.6 \times 10^{-10}$, SpikeyGi2 vs ASAP3; $P = 7.7 \times 10^{-5}$, SpikeyGi2 vs SpikeyGi). By contrast, sensitivity to transient 40-mV step hyperpolarization was stronger for ASAP3 ($\Delta F/F_0$ for SpikeyGi2, $13.0 \pm 1.1\%$, $n = 6$ cells; $\Delta F/F_0$ for SpikeyGi, $-8.7 \pm 1.2\%$, $n = 8$ cells; $\Delta F/F_0$ for ASAP3, $51.4 \pm 4.2\%$, $n = 8$ cells, Student's t-test; $P = 1.1 \times 10^{-7}$, ASAP3 vs SpikeyGi; $P = 5.3 \times 10^{-6}$, ASAP3 vs SpikeyGi2). The fluorescence time course qualitatively differed in SpikeyGi compared with ASAP3 with an overshoot in response at the onset and offset of the voltage step (Fig. 1d). These dynamics could be a consequence of either HEK293 cell expression or photophysics from one-photon excitation[15]. Recordings of spontaneous action potential activity in cultured neurons expressing SpikeyGi and SpikeyGi2 using one-photon excitation produced robust action-potential-related responses (Extended Data Fig. 1)

In vitro characterization of SpikeyGi and SpikeyGi2

To test SpikeyGi and SpikeyGi2 in mouse brain slice preparations, we used simultaneous whole-cell patch-clamp electrophysiology and two-photon imaging of layer 2/3 neurons in primary somatosensory cortex (S1). We imaged single neurons under high-photon flux with an 80-MHz laser[10,16] (Fig. 2a; Methods). SpikeyGi2 showed larger magnitude fluorescence changes than SpikeyGi and ASAP3 to 120-mV depolarization voltage steps from a −70-mV holding potential ($\Delta F/F_0$ for SpikeyGi2, $92.2 \pm 16.0\%$; $\Delta F/F_0$ for SpikeyGi, $41.6 \pm 4.4\%$; $\Delta F/F_0$ for ASAP3, $-29.3 \pm 2.6\%$; Student's t-test, $P = 0.011$, SpikeyGi2 vs SpikeyGi; $P =$

0.0023, SpikeyGi2 vs ASAP3) (Fig. 2b,c). Fluorescence time courses to voltage steps were qualitatively similar between ASAP3, SpikeyGi and SpikeyGi2.

We next compared single action potential responses triggered at 100-ms intervals (Fig. 2d). Line scans were performed along the cell membrane. SpikeyGi2 exhibited greater magnitude peak responses compared with ASAP3 (F/F_0 for SpikeyGi2, 20.4 ± 2.0%; F/F_0 for SpikeyGi, 16.9 ± 2.0%; F/F_0 for ASAP3, −16.1 ± 1.1%; Student's t-test, P = 0.03; Fig. 2e). All three GEVIs showed similar rise times (Fig. 2f). The decay time of SpikeyGi2 was slightly longer than ASAP3 (τ_{decay} for SpikeyGi2, 29.3 ± 2.7 ms; τ_{decay} for SpikeyGi, 26.8 ± 3.1 ms; τ_{decay} for ASAP3, 23.2 ± 2.2 ms; Student's t-test, P = 0.048; Fig. 2g). Despite this, SpikeyGi2 was able to report high-frequency spike trains of 20 and 50 Hz, similar to SpikeyGi and ASAP3 (Fig. 2h). Additionally, we recorded spiking activity in SpikeyGi2-expressing neurons in the anterior olfactory nucleus and the main olfactory bulb (Extended Data Fig. 2). Overall, both SpikeyGi and SpikeyGi2 are capable of reporting single action potentials under high-photon flux.

SMURF two-photon microscope design and performance

We designed a SMURF two-photon microscope capable of imaging a 400 μm × 400 μm FOV at 1 kHz. Although existing fast-scanning microscopes operate in a high-photon flux regime, we sought to construct a 'low-photon flux' excitation system (Fig. 3a). As two-photon excitation uses pulsed lasers, pulse repetition rate determines the total excitable FOV per time bin. To increase the FOV while ensuring one pulse is delivered per voxel, the effective repetition rate of the microscope can be increased proportionally using either temporal or spatial multiplexing. Temporal multiplexing creates multiple delayed excitation beamlets such that the resulting fluorescence detected by a single photomultiplier tube (PMT) is resolved by their timing[17–20]. This approach is limited by the fluorophore's fluorescence lifetime, placing an upper limit on the effective repetition rate. By delivering multiple pulses into different FOV regions simultaneously, the effective repetition rate is not limited during spatial multiplexing[9,21]. However, spatial detectors with cameras or multianode PMTs (MAPMTs) are required for spatial multiplexing. Consequently, crosstalk between neighboring detectors increases with depth because of scattered fluorescence, but this can be reduced by increasing beamlet spacing.

To maximize the effective repetition rate, spatial multiplexing and temporal multiplexing were combined in our SMURF two-photon microscope (Fig. 3b and Extended Data Fig. 3). For excitation, we selected a 920-nm, 31.25-MHz fiber laser that enables 4× temporal multiplexing at 8-ns intervals, providing minimal crosstalk for GFP-based indicators. Compared with 80-MHz Ti:sapphire lasers, lower repetition rate provides >2.5 times greater pulse energy at equivalent average power for more efficient excitation[22]. Each temporally multiplexed beamlet was split into spatially multiplexed beamlet pairs, positioned 200 μm apart at the sample to minimize scatter-related crosstalk. This generated eight beamlets (four temporal × two spatial) with an effective 250-MHz repetition rate. A resonant mirror with 24-kHz line rates was used for fast raster x-scanning. Beamlets were linearly arranged along the slower y axis scanned by a galvanometric mirror. The four (1, 2, 3, 4) temporally multiplexed beamlet pairs (A, B) were spaced 50 μm apart at the sample (Fig. 3c). Each

beamlet scanned a 400 μm × 50 μm subarea, tiling a total area of 400 μm × 400 μm. The patterning of the beamlets with respect to the resonance scanner position produced a slight *x*-axis offset for each subarea. By scanning 24 lines per subarea either unidirectionally or bidirectionally, we achieved 803-Hz or 1,000-Hz frame rates, respectively. The imaging plane was projected onto a commercially available linear 16-anode PMT. Although 2 anodes sufficiently resolve spatially multiplexed beams pairs, 16 anodes provide flexibility in rejecting scattered fluorescence. Signals from 16 anodes were first summed into four detector subgroups (W, X, Y, Z). As beams are temporally multiplexed, detectors are temporally gated to reduce fluorescence from neighboring beamlet pairs (that is, spatial crosstalk detected in subgroup X can be rejected when beamlets 1A and 1B excite the sample). Finally, temporally multiplexed beams assigned to the same detector can be demultiplexed (that is, beamlets 1A and 2A are temporally demultiplexed from subgroup W).

To confirm subcellular resolution performance in each subarea, the point spread function (PSF) of each beamlet was measured using fluorescent beads (n = 7–11 beads per beam; Fig. 3d and Extended Data Fig. 4). Across all subareas, the microscope achieved an average PSF of 0.9 ± 0.1 μm (x)/1.1 ± 0.1 μm (y) lateral resolution and 4.1-μm $\pm$ 0.4-μm axial resolution. We measured the temporal and spatial crosstalk in a cranial-window-implanted mouse virally expressing SpikeyGi in S1. For each beam and detected subareas, SpikeyGi fluorescence was measured across the cortical depth (Fig. 3e and Extended Data Fig. 5). Spatial multiplexing-related crosstalk increased with imaging depth but remained <10% down to 300 μm below the pial surface. Temporal multiplexing-related crosstalk remained <5%, independent of imaging depth. Overall, this demonstrates that the SMURF two-photon microscope can achieve large FOV kilohertz frame scan imaging into deep tissue.

DeepVID improves action potential detection below shot-noise limits

As the SMURF two-photon microscope increases the FOV while maintaining a high frame rate, photon flux is magnitudes lower than high-photon flux regimes. Each neuron receives only approximately 200 pulses per ms, assuming a photon flux of approximately 0.1 μs μm^{-2} (dwell time per voxel). Under such conditions, shot noise dominates pixelwise measurements. We built on a recently developed self-supervised deep convolutional neural network that removes independent noise in calcium imaging data without ground-truth measurements and extended it to denoise voltage imaging data (DeepVID; Fig. 4a)[23,24]. DeepVID combines self-supervised denoising frameworks that infer the underlying fluorescence signal based on a learned model of the independent temporal and spatial statistics of PMT measurements attributed to shot noise[23,25]. Model parameters were chosen based on the image acquisition rate to maximize inference accuracy while preserving the action potential rise time kinetics of SpikeyGi and SpikeyGi2. We first assessed the frame-to-frame variability in fluorescence signal in the raw data and confirmed that pixel fluctuations were proportional to the square root of the mean fluorescence (Fig. 4b), as expected for shot-noise-limited signals. We then compared frame-to-frame variability in the raw data with DeepVID and a conventional temporal filter using a seven-frame moving average. DeepVID reduced the frame-to-frame variability, resulting in a 15-fold improvement in SNR when comparing denoised and raw image data, which is greater than

with a moving average (SNR, 0.501 ± 0.001; raw, 1.316 ± 0.002; moving average, 7.472 ± 0.010; DeepVID, $n = 8,000$ pixels) (Fig. 4c). By breaking this fundamental noise constraint, the underlying fluorescence signal can be more accurately inferred at individual time points (Fig. 4d). Analysis of denoising performance across different frequency bands and under simulated brain motion[26] showed that DeepVID selectively suppressed signals at unwanted frequencies not relevant for spike detection (Extended Data Fig. 6).

To assess how DeepVID improves voltage imaging spike detection reliability, we measured neuronal responses using SpikeyGi in S1 during whisker stimulation. Air puff whisker deflections produce well-timed single action potential responses in layer 2/3 neurons[27]. We delivered single or trains of five air puffs to the contralateral whisker pad and compared raw and denoised fluorescence traces. Denoised traces readily allowed for the identification of potential sensory-evoked and nonevoked spiking events (Fig. 4e). Fluorescence traces were converted into time series of SNR for spike detection (Fig. 4f). Denoising improved the SNR of putative spike events. Analysis of the fluorescence response to single air puffs in denoised versus raw traces shows that peak responses were increased in denoised traces because of better estimates of the baseline fluorescence levels ($\Delta F/F_0$ for raw, $9.3 \pm 0.6\%$; $\Delta F/F_0$ for denoised, $11.1 \pm 0.4\%$; Student's t-test, $P = 2.3 \times 10^{-5}$; Fig. 4g,h). We compared the percentage of putative sensory-evoked spikes detected at varying SNR thresholds before and after DeepVID (Fig. 4i). SNR improvements should reduce the fraction of detected spikes at low SNR thresholds while increasing the fraction of detected spikes at high SNR thresholds. Indeed, compared with raw traces, detected spikes were reduced at low SNR levels (<3) and increased at high SNR thresholds (>3) for traces after DeepVID. Overall, these results demonstrate that shot-noise reduction provided by DeepVID substantially improves the reliability of spike detection in two-photon voltage imaging data.

Positive-going GEVIs outperform negative-going GEVIs in vivo

Using DeepVID, we compared in vivo responses of SpikeyGi and SpikeyGi2 to ASAP3. Cells were imaged across the full FOV at similar laser power compared with in vitro conditions (~30 mW per beamlet) but at lower resolution (x, 1.0 μm per pixel; y, 2.1 μm per pixel). Using the SMURF two-photon microscope, we simultaneously imaged >100 neurons and could identify sensory-evoked action potentials (SNR > 4) to both single and trains of air puffs (Fig. 5b,c and Extended Data Fig. 7). We compared the fluorescence responses to single air puffs (Fig. 5c). SpikeyGi and SpikeyGi2 showed larger peak responses compared with ASAP3 ($\Delta F/F_0$ for SpikeyGi2, $13.4 \pm 0.1\%$; $\Delta F/F_0$ for SpikeyGi, $10.1 \pm 0.1\%$; $\Delta F/F_0$ for ASAP3, $7.9 \pm 0.1\%$; Student's t-test, $P = 0.004$, SpikeyGi2 vs ASAP3; $P = 0.006$, SpikeyGi2 vs ASAP3). Simultaneous in vivo electrophysiology and imaging recordings provided some indication of GEVI performance under low-photon flux regimes (Extended Data Fig. 8). As SNR can vary from cell to cell because of tissue inhomogeneity and indicator expression, we evaluated sensor performance across the neuronal population as a function of SNR. For SpikeyGi and SpikeyGi2, we observed that spike detection using 4–4.5 SNR thresholds yielded similar sensory-evoked and spontaneous spike rates compared with previously reported values in layer 2/3 S1 neurons from in vivo whole-cell recordings[28] (Fig. 5d). For ASAP3, sensory-evoked firing rates were lower compared with SpikeyGi and SpikeyGi2, suggesting underdetected spikes in similar imaging conditions. We evaluated

the temporal fidelity of SpikeyGi and SpikeyGi2 responses to 5-Hz to 10-Hz trains of air puffs. As spiking probability to whisker stimulation is variable in layer 2/3 S1 neurons, we generated average traces to detected action potentials for each air puff in the stimulus train (Fig. 5e). At both 5-Hz and 10-Hz stimulation frequencies, averaged traces show well-isolated spike responses to each air puff within the stimulus train. These results demonstrate that SpikeyGi and SpikeyGi2 in combination with the SMURF two-photon microscope are suitable for population-level voltage imaging.

Low-photon flux enables sustained in vivo voltage imaging

Finally, we assessed the capacity to perform sustained in vivo voltage imaging at low-photon flux with the SMURF two-photon microscope. We compared photobleaching rates in vivo at low-photon flux conditions using the SMURF two-photon microscope under intermittent (9 s on, 4 s off) or near continuous (59 s on, 1 s off) imaging conditions across 60 min (Fig. 6a and Extended Data Fig. 9). Although continuous imaging resulted in similar degrees of photobleaching for SpikeyGi2 and ASAP3, intermittent imaging resulted in less photobleaching for SpikeyGi2, suggesting different photorecovery properties. We assessed how photobleaching affects spike signals in positive-going indicators (Fig. 6b,c). Overall, we found no significant difference in spike detection across 60 min when during continuous ($P = 0.63$, $F_{4,570} = 0.64$, one-way analysis of variance (ANOVA) with post-hoc multiple comparison test) and intermittent ($P = 0.68$, $F_{4,350} = 0.60$, one-way ANOVA with post-hoc multiple comparison test) imaging conditions.

Given that the SMURF two-photon microscope delivers a total of 240 mW across eight beams, we tested for photodamage after 1 h of sustained in vivo imaging[13]. Temperature measurements using thermocouple probes positioned in the excited tissue area never exceeded 32 °C after 1 h of photoexcitation (Fig. 6d). Brains were perfused 16 h after imaging and immunostained for markers of tissue damage: astrocytic (anti-GFAP), microglial (anti-Iba1), heat shock (anti-HSP-70/72) and apoptotic pathway activation (anti-caspase-3). We measured average fluorescence levels in the laser-exposed and control areas of the cortex (Fig. 6e). Laser exposure did not produce any significant difference between laser-treated and control areas for any of the markers (GFAP, $t = 2.27$, $P = 0.11$; Iba1, $t = 0.06$, $P = 0.95$; HSP, $t = 1.75$, $P = 0.18$; caspase-3, $t = 0.39$, $P = 0.72$; paired Student's t-test, $n = 4$). In summary, low-photon flux imaging using the SMURF two-photon microscope and positive-going GEVIs provides safe and sustained population-level voltage imaging.

Discussion

By combining the following innovations, we demonstrate sustained large-scale, fast, two-photon voltage imaging from large sets of neurons in awake mice. We developed GEVIs with a positive fluorescence–voltage slope relationship (SpikeyGi and SpikeyGi2) with increased voltage responses for improved spike detection of high-frequency spike trains up to 50 Hz. We developed the SMURF two-photon microscope, combining temporal and spatial multiplexing to increase the effective pulse rate of the excitation source while maintaining low-detection crosstalk. We were able to achieve kilohertz frame scanning in deep tissue at twice the FOV of current kilohertz-scanning two-photon systems

(Supplementary Table 1). With low-photon flux excitation, we reduced photobleaching and photodamage, enabling sustained and chronic voltage imaging. To improve spike detection at low-photon flux levels, we developed a self-supervised, deep learning denoising method (DeepVID). DeepVID denoising was achieved without sacrificing spatial or temporal resolution and without access to ground-truth high SNR measurements. We achieved improvements in SNR comparable to similar denoising methods applied to two-photon calcium imaging data[23,24].

These combined tools represent a new direction for scaling up two-photon voltage imaging. For the SMURF two-photon microscope, FOV can be further increased while maintaining photon budget by additional judiciously placed spatially multiplexed beamlets to increase the effective repetition rate and beam shaping to improve excitation efficiency[29,30]. DeepVID can be improved by incorporating more advanced network architectures, such as spatiotemporal convolution and attention module[31]. Improving the response amplitude of GEVIs by decreasing resting fluorescence and improving subcellular localization to reduce background will allow subthreshold measurements while maintaining a large FOV. Overall, low-photon flux imaging pushes the boundaries for monitoring neuronal activity across spatial and temporal scales.

Online content

Any methods, additional references, Nature Portfolio reporting summaries, source data, extended data, supplementary information, acknowledgements, peer review information; details of author contributions and competing interests; and statements of data and code availability are available at https://doi.org/10.1038/s41592-023-01820-3.

Methods

Plasmid construction

Starting constructs, pcDNA3.1/Puro-CAG-ASAP3b and pcDNA3.1/Puro-CAG-ASAP3b-Kv2.1, were a generous gift from Michael Z. Lin (Stanford University)[5]. A self-cleaving T2A peptide sequence (GSGEGRGSLLTCGDVEENPGP) followed by nuclear-localized tag fluorescent proteins (mCherry) at the C terminus of ASAP3 was added to identify the expressing cells during functional screening. For neuronal expression, SpikeyGi and SpikeyGi2 were subcloned into the pAAV-hSyn-eGFP (Addgene no. 50465) by replacing eGFP using KpnI and NheI restriction sites. Additionally, a fusion of the C-terminal cytoplasmatic segment of the Kv2.1 channel (the 65-amino-acid-long proximal restriction and clustering signal) via the GSSGSSGSS linker restricted SpikeyGi and SpikeyGi2 expression to the soma and proximal dendrites[5]. All constructs were manufactured using the InFusion Cloning System (Takara Bio), with all of the products confirmed by sequencing (Keck DNA Sequencing Facility).

Virus production

AAV2/PhP.eB-hSyn-SpikeyGi-Kv2.1 (9.7×10^{12} genome copies (gc) per ml) was obtained from Boston Children's Hospital Viral Core. AAV2/8-hSyn-SpikeyGi-Kv2.1 (1.0×10^{10} gc per ml) and AAV2/8-hSyn-SpikeyGi2-Kv2.1 (1.0×10^{10} gc per ml) were produced and

purified in-house using an established protocol[32] and commercial purification and titration kits (Takara Bio).

Library production

The production of GEVI site-directed mutagenic libraries has been described previously[14,33]. In brief, the mutagenic PCR reaction was performed with three forward primers containing three degenerative codons (NDT, VHG and TGG) and a single reverse primer. This combination of degenerate primers resulted in site-directed mutagenic libraries encoding all 20 amino acids with repeats for two amino acids: lysine and valine. The insertional library that resulted in the development of the SpikeyGi was produced with a single set of PCR primers with the forward primer containing degenerate codon NNKNNK targeted between ASAP3 amino acid residues D151 and N152 (ref. [5]). The 15-bp-long overlapping extension with a sequence identical to a vector at the insertion site in forward primers facilitated vector circularization. CloneAmp DNA polymerase was used for the PCR reaction. The parent template was removed with DpnI restriction enzyme digestion. In-Fusion HD enzyme premix (Takara Bio) was used for ligating amplified mutagenic vectors. Stellar Chemically Competent Cells (Takara Bio) were used for bacterial transformation. Mutagenic libraries were produced in the 96-well plate with 46 bacterial colonies selected for each (two libraries per 96-well plate; four wells were controls). cDNA was purified using an automated liquid handling robot (epMotion 5057; Eppendorf), and the library complexity was confirmed by sequencing 10% of selected colonies. Initial site-directed mutagenesis targeted six amino acid residues in ASAP2f (L145, S146, F147, N148, S149 and H150; numbering from the starting Met of ASAP2f)[10]. The insertional library that resulted in the insertion of two amino acid residues (DS) to create the SpikeyGi was targeted between residues D151 and N152 in ASAP3. To create SpikeyGi2, we screened several other residues in the linker region between the voltage-sensing domain and FP (R149, G150 and D151) and within the FP (N167, F168 and V170; all numbering from the starting Met in ASAP3). The full primer list is shown in Supplementary Table 2.

Maintenance and transfection of HEK293 cell lines

Functional testing on the semiautomated screening platform was performed on spontaneously spiking HEK293 cells (a kind gift from Adam Cohen, Harvard University[34]; no. CRL-326, ATCC) expressing GEVI mutants. Stable expression of NaV1.3 and KiR2.1 ion channels induces spike-like electrical activity in these cells. Cells were cultured in DMEM/F12, 10% FBS, geneticin (500 µg ml^{-1}) and puromycin (2 µg ml^{-1}) (Sigma-Aldrich). HEK293 cells (no. CRL-1573, ATCC) were used for simultaneous voltage-clamp recording and widefield imaging. The cells were kept in DMEM (high glucose; Invitrogen) supplemented with 10% FBS. Cells were kept in a humidified incubator at 37 °C in a 5% CO_2 environment and were used for up to 25 passages. For functional testing, cells were plated either on glass-bottom 96-well black dishes (screening platform; Cellvis) or on 12-mm coverslips (electrophysiology experiments, Carolina Biological) coated with poly-d-lysine (Sigma-Aldrich). Transient expression of GEVI variants in HEK293 lines was performed using Lipofectamine 2000 (0.25 µl per 96-well dish or 1 µl per 24-well dish, Invitrogen) with plasmid DNA (0.2 µg per 96-well dish or 0.4 µg per 24-well dish). Experiments were performed 48–72 h after transfection.

Primary neuronal cultures

All experiments were carried out in strict accordance with the protocol approved by the Pierce Animal Care and Use Committee (VP1–2022). The cortical and hippocampal neurons were dissected from pregnant CD-1 dams at embryonic day 18 (E18) followed by digestion in 0.25% Trypsin (Invitrogen) for 30 min at 37 °C. Neurons were dissociated by gentle trituration in Neurobasal/10% FBS medium. Neurons were plated in Neurobasal medium supplemented with 10% FBS, 2% B27 and 2 mM GlutaMAX (Thermo Fisher) at a density of 120,000–150,000 cells per coverslip on 12-mm coverslips coated with poly-d-lysine hydrobromide (Sigma-Aldrich). After 24 h, the plaiting medium was replaced with culturing medium (Neurobasal medium, supplemented with 2 mM GlutaMAX and B-27 supplement). Cells were kept in a humidified incubator at 37 °C in a 5% CO_2 environment. For neuronal expression of GEVIs, the 12-mm coverslips plated with 120,000–150,000 neurons were treated with 1 μl of adeno-associated virus (AAV) viral particles prepared in-house on days in vitro (DIV) 9. The functional imaging experiments were performed on DIV 14–20.

Functional testing of mutagenic libraries with one-photon imaging

The functional screening of GEVI mutants was performed as previously described[14,33]. In short, a semiautomated screening platform was built around a Nikon Eclipse Ti-E inverted microscope equipped with a Perfect Focus System and a motorized Prior Proscan II stage (Prior Scientific). The custom-made imaging chamber holds 96-well plates under constant temperature (37 °C) and humidity during experiments. Imaging was performed using a Nikon Plan Apo 20 × 0.75 NA objective (Nikon), a pE-300 (CoolLED) light source, and an ORCA Flash 4.0 scientific CMOS camera (Hamamatsu). A 470/40-nm excitation filter, 495-nm dichroic mirror, and 525/25-nm emission filter (no. 49002, Chroma Technologies) were used to image green fluorescence. The nuclear-localized tag protein, mCherry, was visualized with a 560/40-nm excitation filter, 585-nm dichroic mirror, and 630/75-nm emission filter (no. 49008, Chroma Technologies). For field stimulation (Grass S48 Stimulator), we used a custom-made field electrode and actuator system (Thorlabs) attached to the roof of the imaging chamber. The image collection, electrical stimulation, and signal detection were done using a custom application written in LabVIEW (National Instruments). The fluorescence intensity of nuclear-localized mCherry was used to identify expressing cells and select for the fields of view within each well. For functional screening, images were collected at 50 fps in 2,500-ms-long sweeps with a single pulse of 70 V at 500 μs applied at 400 ms from the beginning. The fluorescence signal in each cell in response to field stimulation was quantified as % F/F_0. Each GEVI variant was screened in four separate plates, and the selection of the best mutants was based on the maximum response amplitude across cells and wells.

Electrophysiology and widefield imaging in HEK293 and primary neuronal cells in vitro

For whole-cell patch-clamp experiments, HEK239 cells were kept in a perfused chamber at 33–35 °C (Warner Instruments) with the constant running bath solution (129 mM NaCl, 4 mM KCl, 1 mM $CaCl_2$, 1 mM $MgCl_2$, 10 mM D-glucose, and 10 mM HEPES, pH 7.4, and was adjusted to 310 mOsm with sucrose). The 3-MΩ to 5-MΩ glass patch pipettes (capillary tubing with 1.5/0.75 mm outer diameter/inner diameter; WPI) were pulled on

a P-97 Flaming/Brown type micropipette puller (Sutter Instrument Company). The pipette solution contained 125 mM K-gluconate, 8 mM NaCl, 0.6 mM $MgCl_2$, 0.1 mM $CaCl_2$, 1 mM EGTA, 4 mM Mg-ATP, 0.4 mM Na-GTP, and 10 mM HEPES, pH 7.2, and adjusted to approximately 290 mOsm. Voltage-clamp recordings in the whole-cell configuration were performed using MultiClamp 700B amplifier, digitizer Digidata Series 1400A, and pClamp software (Molecular Devices). Depending on the experiment, the voltage was changed from a holding potential of −70 mV to either +30 mV (a 100-mV single-step depolarization experiment), or −110, −90, −50, −30, −10, 10 and 30 mV (in a series of 20-mV incremental subsequent steps). Each epoch was 1 s long, with an initial and final resting interval of 200 and 500 ms, respectively, and a voltage step of 300 ms. The sensitivity of all tested GEVIs was sufficient for single-trial signal detection.

The experiments with primary neuronal cultures in vitro were performed under the same conditions but with a modified pipette solution (120 mM K-gluconate, 3 mM KCl, 7 mM NaCl, 4 mM Mg_2^+-ATP, 0.3 mM Na-GTP, 20 mM HEPES and 14 mM Tris-phosphocreatine; pH adjusted with KOH to pH 7.3). To record spontaneous neuronal activity, neurons were kept in neutral mode following whole-cell membrane rupture. The resting membrane potential of active cells was between 35 and 45 mV. The neurons were recorded in 10- to 20-s-long epochs at 500 fps. Imaging was performed on an Olympus BX61WI upright microscope using a LUMPlan FL 40× NA 0.80 water immersion objective (Olympus) and 488-nm, 50-mW laser light excitation (DL488–050). We used a GFP filter set, a 495-nm dichroic mirror, and a 520/35-nm emission filter (Semrock), and the laser power measured at the preparation was 20–23 mW mm^{-2}. Additionally, the light intensity was adjusted for each recording session using a continuous circular neutral density filter (Thorlabs) to the minimum required to record optical signals. The images were collected with a fast-speed NeuroCCD camera controlled by NeuroPlex software (RedShirt Imaging) at 500 or 1,000 Hz. For the image demagnification, we used either an Optem zoom system A45731 0.13 or Optem C-to-C mount 25–70-54 0.383 (Qioptiq LINOS).

Widefield imaging analysis

The data were analyzed using NeuroPlex, Excel and custom scripts written in Igor and Matlab. All of the results from experiments that combined optical imaging and electrophysiology are presented as a mean value and s.e.m. The optical traces are spatial averages of the intensity of the pixels within the region of interest (ROI) that covers the cell membrane. The ROIs were visually identified using the Neuroplex feature Frame Subtraction. For bleach correction, the portion of the trace outside the stimulus was fitted with a double exponential curve. The amplitude of fluorescence change was measured as the difference between the averaged values for 50 frames before stimulation and 3 (for SpikeyGi and SpikeyGi2) and 100 (ASAP3) frames around the peak of the response. Data are presented as % F/F_0.

Animal preparation

All experimental procedures were approved by the Institutional Animal Care and Use Committee for the Charles River Campus at Boston University (PROTO201800532). For in vitro slice experiments, viral injections were performed in 18 male and female neonatal

(P7-P9) C57BL/6 mice. Mice were bred in-house in the Boston University animal care facility, with standard housing, a 12-h light/dark cycle, and ad libitum access to food and water. Pups were removed from the mother, anesthetized with 1%–3% isoflurane, and placed in a custom stereotaxic holder for neonatal mice. A small incision was made in the scalp, and two small holes were made with a 30-gauge needle in the skull of the left hemisphere. Mice were injected with 300 nl AAV2/PhP. eB-hSyn-SpikeyGi-Kv2.1 (1:4 in saline), AAV2/8-hSyn-SpikeyGi2-Kv2.1 (1:2 in saline), or AAV2/1-hSyn-ASAP3b-kv-WPRE (1:4 in saline) at 250 μm below the pial surface. Incisions were closed with Vetbond Tissue Adhesive (3 M), and animals were treated postoperatively with buprenorphine (0.05–1 mg kg^{-1}, subcutaneously). Animals were returned to their mother immediately after surgery and weaned at 3 weeks of age. For in vivo experiments, male and female adult (6- to 8-week-old, 7 total) C57BL/6 mice (Charles River Laboratories) had stereotaxic viral injections of GEVIs in layer 2/3 and L5 of primary somatosensory cortex, 300 and 500 μm below the pial surface (600 nl total volume). AAV2/PhP. eB-hSyn-SpikeyGi-Kv2.1 (1:4 in saline), AAV2/8-hSyn-SpikeyGi2-Kv2.1 (1:2 in saline) or AAV2/1-hSyn-ASAP3b-kv-WPRE (1:8 in saline) was injected. There were two injection sites per mouse, both targeting the left hemisphere sensorimotor (S1) cortex (AP, –1.1 mm, ML, 2.9 mm; and AP, –1.1 mm; ML, 3.3 mm). To enable optical access, a 4-mm cranial window was implanted over S1. A metal headpost was implanted over the right hemisphere to enable head fixation. Animals were treated postoperatively with buprenorphine (0.05–1 mg kg^{-1}, subcutaneously) and given 2–3 weeks for viral expression to take place. Animals were handled and habituated to head fixation for 3–5 days before imaging experiments began.

Slice electrophysiology

For in vitro characterization of GEVIs, whole-cell slice electrophysiology was performed on layer 2/3 S1 neurons of 18 male and female neonatal (P7–P9) C57BL/6 mice that had received cortical viral injections of SpikeyGi, SpikeyGi2 or ASAP3 3–4 weeks before recording. Slice electrophysiology was also performed in the main olfactory bulb (MOB) and accessory olfactory nucleus (AON) neurons in a separate group of C57BL/6 mice that received viral injections of SpikeyGi2 in the MOB and AON 3–4 weeks before recording. To obtain brain tissue slices, mice were deeply anesthetized with pentobarbital or ketamine/ xylazine and transcardially perfused with modified artificial cerebrospinal fluid (in mM, 87 NaCl, 75 sucrose, 10 glucose, 2.5 KCl, 1.25 NaH$_2$PO$_4$, 25 NaHCO$_3$, 1.3 ascorbic acid, 0.5 CaCl$_2$ and 7 MgCl$_2$). Brain tissue was sliced into 300-μm coronal sections and maintained with oxygenated (95/5% O$_2$/CO$_2$) artificial cerebrospinal fluid (in mM, 124 NaCl, 26 NaHCO$_3$, 3 KCl, 1.25 NaH$_2$PO$_4$, 2 CaCl$_2$ and 1.5 MgCl$_2$). Pipettes were pulled from thin-walled borosilicate capillaries without filament (3–6 MΩ) (Sutter Instruments) and filled with internal solution (in mM, 135 K-gluconate, 5 KCl, 10 HEPES, 2 MgCl$_2$, 4 MgATP, 0.1 EGTA, 0.5 Na$_3$GTP, 4 phosphocreatine disodium). For layer 2/3 cortical neurons, the process of approaching the cell, sealing onto the membrane, and breaking in to establish a whole-cell configuration was controlled by Autopatcher (Neuromatic Devices). For MOB neurons, suction was applied manually to create a seal and establish a whole-cell configuration. Electrical signals were recorded with a Multiclamp 700B amplifier (Axon Instruments), filtered at 3 kHz and digitized at 20 kHz (National Instruments PCI-6321), and recorded with custom MATLAB software (Mathworks). Simultaneous two-photon imaging

was performed with a conventional two-photon microscope (Ultima, Prairie Technologies) using a 40×/0.8 NA water immersion objective (Olympus) and Dodt contrast imaging. For laser source, an 80-MHz Ti:sapphire laser (Mai Tai HP, Spectra Physics) was tuned to 920 nm with 35–45 mW delivered at the sample.

For layer 2/3 S1 neurons, fluorescence responses to membrane potentials were performed while neurons were held in voltage-clamp mode. One-second trials consisted of a 200-ms baseline period at resting membrane potential (approximately –70 mV), followed by a 400-ms voltage steps and then a return to resting membrane potential for 400 ms. Trials were repeated 10 times across 10 voltage steps ranging from –130 to +50 mV (20-mV increments). For image acquisition, frame scans of the targeted cell were acquired at 20 Hz across 140×104 pixels at ~0.6-μm per pixel resolution and 2.8-μs pixel dwell time. The targeted cell received approximately 5×10^5 pulses per 50-ms time bin. For analysis, the cell membrane was segmented by isolating pixels 1.3–2.0 times above background. For characterization of action potential responses, neurons were recorded in current-clamp mode with a single action potential evoked by 2-ms to 5-ms pulses of 1,200–2,000 pA, with ten 500-ms sweeps of 5–25 action potentials each. Fluorescent responses were recorded by line scans along the cell membrane at 17–108 pixels per line, scanned at 2.5–6 kHz, and a 1.6-μs to 2.8-μs pixel dwell time. Fluorescent recordings were filtered for 60-Hz noise and resampled to 2 kHz for analysis. For characterization of action potential responses in MOB and AON neurons, recordings were performed in current-clamp mode. Action potentials were evoked by current injection (600–800 pA, 5 ms). Line scans were recorded with 137–172 pixels per line, scanned at 1.10–1.33 kHz, with 4.8 μs per pixel dwell time equivalent to approximately 9,000 excitation pulses per 1-ms time bin. F/F_0 was calculated, where F_0 corresponded to fluorescence at resting membrane potential.

Microscope design

The optical design was performed using Zemax OpticStudio software (Zemax LLC), and the opto-mechanical design was performed using AutoDesk Inventor (Autodesk). A 920-nm, 2-W fiber laser (ALCOR-920; Sparks Lasers; 100-fs pulse duration, 31.25-MHz repetition rate) was used as the light source. The total laser power was controlled by a Pockel's Cell (350–80; ConOptics). The laser beam was split into four beam paths using polarizing beamsplitter (PBS) cubes (PBS123/CCM1-PBS253; Thorlabs). A half-wave plate (AHWP05M-980; Thorlabs) was placed before each beamsplitter cube (three in total) to allow power control of individual paths. Two half-wave plates were mounted on manual rotation mounts (CRM1PT/M and PRM05/M; Thorlabs) The third half-wave plates were mounted on a motorized precision rotation stage (PRM1/MZ8; Thorlabs) for remote control when selecting between eight beams and one beam imaging. Temporally multiplexed beams were delayed by 8 ns relative to each other using delay lines. After the delay line, all beams were reduced to obtain a 1.5-mm beam diameter (BE052-B, AC127–075-B, ACN127–025-B or BE02–05-B; Thorlabs).

Temporally multiplexed beams were routed into customized beamsplitter plates. Beamsplitter plates serve two functions. First, they split each temporally multiplexed beam into pairs of spatially multiplexed beams. Second, they arrange the beamlets linearly to

define the position of each subarea. A beamsplitter plate consisted of an assembly of half-wave plates (AHWP05M-980; Thorlabs) on rotation mounts (PRM05/M; Thorlabs), PBS cubes (PBS123 and PBS053; Thorlabs) and half-inch gold-coated mirrors (PF05–03-M01; Thorlabs) on miniature mirror holders (LMMH-12.7R-N; OptoSigma). One beamsplitter routed four beams through independent f = 100-mm relay lenses (KPX034AR.16; Newport) that were held in a customized lens holder and separated by 8.5 mm, corresponding to 100-μm spacing at the sample. Two beamsplitter plates were used to combine a total of eight beams using a 2-in. PBS cube (PBS513; Thorlabs) and positioned such that beams from each beamsplitter plate were interleaved at 50-μm spacing at the sample. A beam blocker mounted onto a linear actuator (L12-P; Actuonix) was placed after each lens holder and allowed selection between all eight beams or any arbitrary individual beam.

All eight beamlets were sent to a customized f = 330-mm scan lens assembly (SLB-50–300N, SLB-50–450P, and SLB-50–250P; OptoSigma) and conjugated to a 12-kHz resonant scanner (CRS 12 kHz, 5.0 mm × 7.2 mm aperture, Cambridge Technology) and galvo scanner (6215H, Cambridge Technology). The scan lens (S4LFT0089/094; Sill Optics) and tube lens (AC508–500-B and AC508–750-B, Thorlabs) expanded the beam to fill the back aperture of the objective (N16XLWD-PF, 16×; Nikon). The laser light was reflected to the objective by a short-pass filter (FF01–720/SP-25, AVR Optics).

The emitted light passed through the short-pass filter and then was separated by a secondary dichroic (FF556-SDi01–40×45; Semrock) into green and red fluorescent channels. Red fluorescence excited from a single beam was detected using an achromatic lens (AC508–080-A; Thorlabs) and an eyepiece (19 mm; Televue) focused onto a hybrid PMT (R11322U-40; Hamamatsu). For green fluorescence, a customized lens assembly was used to magnify and reshape the square FOV to match the geometry of a 16 × 1 multianode photomultiplier (H13123, GaAsP 16-channel MAPMT; Hamamatsu). The assembly included two achromatic lenses (AC508–100-A; Thorlabs) and two cylindrical lenses (LJ1567RM-A, Thorlabs; CKX019, Newport) positioned orthogonal to each other.

Using a customized 16-to-4 adder (Marina Photonics), signals from the 16 MAPMT anodes were amplified, digitized and combined into four detector subgroups each consisting of signals from four adjacent anodes. Using custom electronics, the subsequent LVPECL signal was converted and fanned out to two LVDS signals (NB6N11S; ON Semiconductor). The signals were collected by a field-programmable gate array (FPGA; PXIe-7965R; National Instruments) with a 20-channel digital I/O board (NI-6587; National Instruments) operating at 1 Gbit s^{-1} sampling rate. For a given detector subgroup, the two fanned out signals were inputted into two I/O channel wherein one of the two fanned out signals was delayed by 0.5 ns. This provided a 2 Gbit s^{-1} sampling rate for each detector subgroup when combined on the FPGA.

Each detector subgroup contained fluorescence from two beamlets that were then temporally demultiplexed on the FPGA using a synchronization signal provided by the laser and electronic delay box (DB64, Stanford Research Systems) providing demultiplexing with 0.5-ns precision. Additional time-dependent gating was implemented on the FPGA to minimize spatial multiplexed crosstalk from neighboring detector subgroups (LabVIEW,

National Instruments). For sample positioning, a lifting stage (HT160–16-DC, Steinmeyer Mechatronik) mounted on an XY stage (KT310–200-DC, Steinmeyer Mechatronik) was used. The microscope system was controlled by customized C++-based software (Scope). The software controlled the resonant and galvo scanner (imaging FOV), the pockel's cell (laser power), and the shutter through a DAQ module (PXI-6259, National Instruments).

Point spread function characterization

For each beamlet in the SMURF two-photon microscope, the PSF was measured using 0.5-μm-diameter fluorescent beads (T7281; Invitrogen). Images were taken one beamlet at a time. The beads were embedded in 1.5% agarose, and an image stack of the bead was taken at 0.1 μm × 0.1 μm × 0.5 μm voxel resolution with 50 frames at each plane. Motion correction was performed at each plane before averaging. A summed Z-intensity projection of the image stack was taken and the maximum intensity pixel was identified as the center of the bead along the x–y axis. The center along the z axis was defined as the plane with the maximum total signal. The profile was plotted through the center along each axis. The PSF value reported was the full-width-at-half-maximum of each profile.

Crosstalk characterization

To determine the degree of temporal and spatial crosstalk observed in scattering tissue, a mouse virally expressing SpikeyGi implanted with a cranial window was used. Tissue was scanned using one beam at a time (~30 mW), and fluorescence was collected across all eight subareas. Images consisting of 50-frame averages acquired at 389 Hz were taken at 30-μm steps from 0 to 300 μm below the pial surface. For the excited subarea in each image, pixels corresponding to SpikeyGi fluorescence were identified as those whose intensities were >95th percentile compared with other pixels in the same subarea. Per cent crosstalk was calculated as the mean signal measured in each of the nonexcited subareas divided by the mean signal in the excited subarea containing SpikeyGi fluorescence.

Intrinsic signal optical imaging

To identify the location of viral expression relative to S1, intrinsic signal imaging was performed in mice under light anesthesia (1%–1.5% isoflurane). The cortical surface was illuminated with a 625-nm light-emitting diode (LED; Thorlabs), and two individual whiskers (B2 or C2) were stimulated at 10 Hz with a piezo-electric stimulator. Reflectance images were recorded using a $f = 25$-mm lens (Navitar) and a CMOS camera with a 30-Hz frame rate, 6.5-μm pixel size, 4 × 4 binning, and 512 × 512 binned pixels (Hamamatsu). Cortical activation in the barrel column was determined by comparing changes in reflectance during whisker stimulation versus periods of nonstimulation, expressed as R/R_0 (150-frame average). Barrel columns were identified as signal minima after averaging intrinsic reflectance signals over 10 trials.

Self-supervised deep learning denoising of voltage imaging data

DeepVID combines self-supervised frameworks implemented in DeepInterpolation and Noise2Void[23,24]. The network architecture of DeepVID was based on the DnCNN[35], a fully convolutional network with residual blocks. This architecture was chosen to better

accommodate the 8:1 aspect ratio in the subimage scanned by each beamlet. The network was constructed with two-dimensional (2D) convolution layers, batch normalization layers, and parametric rectified linear unit (PReLU) activation layers, with 16 repeated residual blocks in the middle. Each residual block contained two 3×3 2D convolution layers with batch normalization layers following, and a PReLU activation layer was appended after the first batch normalization layer. The skip connection was added to link low-dimensional and high-dimensional features by adding the feature map of the input and the output for each residual block (Fig. 4a). DeepVID was designed to denoise a single frame from each subarea at a time. It was trained to predict the central frame N_0 using an input image time series, consisting of N_{pre} frames before and N_{post} frames after the central frame, in addition to a degraded central frame with several 'blind' pixels. A random set of pixels (p_{blind}) in the central frame were set as blind pixels using a binary mask, whose intensities were replaced by a random value sampled from randomly selected pixels in the frame. The hyperparameters ($N_{pre} = 3$, $N_{post} = 3$, $P_{blind} = 10\%$) were optimized to maintain the temporal dynamic of voltage signal spikes while recovering a high single-frame spatial resolution. The loss function was the mean squared error (that is, L2 loss) between the original and denoised central frame and was calculated only on the blind pixels. The training was performed using the Adam optimizer with 360 steps per epoch and a batch size of four. The training stopped after going over all samples in the data set three times to avoid overfitting. The learning rate was initialized at 5×10^{-6} and reduced to 1×10^{-6} when the loss on the validation set did not decrease in the last 288,000 samples.

The training data set consisted of 1,181 videos, each of which contained 1,000 frames acquired at 803 Hz. Each image time series was preprocessed by detrending and normalization before sending into the DeepVID network. For detrending, the trend was approximated by a second-order estimator by fitting to the time trace of the intensity mean of each frame. The scalar in the trend at each frame was subtracted from all of the pixels in the corresponding frame. The detrended video was then normalized by subtracting the mean and dividing by the s.d. of all pixels in the image time series. The network was trained on a graphics processing unit (Nvidia P100, 12 GB VRAM) using TensorFlow 2.2.0, Python 3.8 and CUDA 11.2. Once DeepVID was trained, inference denoising of subsequent image data using the trained model was performed frame by frame, by feeding each corresponding seven-frame image time series. It can be performed at approximately 200 frames per second on a single Nvidia P100 GPU. To quantify the performance of DeepVID, the single-pixel SNR was defined as the ratio of the mean divided by the standard deviation of the pixel intensity along the temporal axis. As a benchmark, raw image data were alternatively denoised by applying a moving average across imaging frames along a window of seven frames, equivalent to the frame window used in DeepVID. Power spectrum density analysis was performed by calculating the average of the squared magnitude of the Fourier transform of the time trace from each pixel.

In vivo electrophysiology

In vivo whole-cell electrophysiology was performed in one head-fixed, anesthetized male adult (6- to 8-week-old) C57BL/6 mouse, 3–4 weeks after viral injection of SpikeyGi2. The mouse was anesthetized with isoflurane (1%–3%). Dental cement was used to attach

a headpost on the right hemisphere and to create a chamber to hold cortex buffer in place over the recording area on the left hemisphere. A small dental drill head (500 μm) was used to thin the skull for a craniotomy (<3-mm diameter), and the last layer of bone (~50 μm) was carefully removed using a 30-G syringe needle. The cement chamber was filled with cortex buffer (in mM, 126 NaCl, 5 KCl, 10 HEPES, 2 $MgSO_4$, 2 $CaCl_2$, 12 glucose), and the dura was carefully lifted and removed. A 3-mm circular glass coverslip was cemented in place over two-thirds of the craniotomy, leaving a 0.5-mm to 1-mm section of brain exposed on the lateral edge of the craniotomy. A layer of 2% low-melt agarose was applied over the exposed brain area. The mouse was then placed on a heating pad, head-fixed under the SMURF two-photon microscope, and remained anesthetized with 1%–3% isoflurane throughout the recording.

A CCD camera (CS165MU/M, Thorlabs) was used to locate the imaging area within the craniotomy. Pipettes were inserted in the exposed section of the craniotomy and advanced until reaching the recording area under the coverslip. Recordings were obtained with 1.5-mm borosilicate glass pipettes (BF150–86-10,Sutter Instruments) controlled by a four-axis micromanipulator (SM10, Luigs & Neumann). Pipettes had a 7-MΩ to 9-MΩ tip resistance and were filled with internal solution (in mM, 135 K-gluconate, 5 KCl, 10 HEPES, 2 $MgCl_2$, 4 MgATP, 0.1 EGTA, 0.5 Na_3GTP, 4 phosphocreatine disodium) containing 50 μM Alexa Fluor 594 (Invitrogen). During targeted patching, SpikeyGi2-expressing neurons and Alexa-Fluor-594-filled pipettes were visualized with the SMURF two-photon microscope by scanning a single 920-nm excitation beam at 50 Hz in combination with green- and red-channel detectors. Positive pressure (50–300 mbar) was applied while the pipette was advanced through the tissue. On contact, manual suction was used to seal the membrane and break into the cell. Voltage imaging was subsequently performed at 803 Hz using multibeam excitation. Electrophysiological signals were amplified with a Multiclamp 700A amplifier (Axon Instruments), filtered at 10 kHz before digitization at 20 kHz (National Instruments) and recorded with Wavesurfer (HHMI Janelia Research Campus).

In vivo voltage imaging

To measure sensory-evoked voltage responses, whisker stimulation was performed on awake, head-fixed mice. Air puffs (25 ms) were delivered to the whisker pad contralateral to the imaged hemisphere. Stimulus patterns consisted of alternating trains of one puff or five puffs separated by 4-s intervals. Trains of five air puffs were delivered at either 5- or 10-Hz stimulus frequency. Using the SMURF two-photon microscope, voltage imaging in S1 was performed at a 803-Hz frame rate across 400×192 total pixels (400×24 per subarea) at x of 1.0 μm per pixel resolution and y of 2.1 μm per pixel resolution, approximately 30 mW per beamlet, and approximately 0.1-μs dwell time. For image analysis, each subarea was analyzed independently in MATLAB (Mathworks). For correction of brain motion, brain motion was estimated using a 2D rigid fast-Fourier transform based on images from one subarea, and then a rigid transform correction was applied to all eight subareas. Images for each subarea were then denoised using DeepVID. Neurons were then manually segmented, and fluorescence traces were extracted for each ROI. Only neurons fully contained within a subarea were segmented. Neurons at the edge of the subareas were excluded from manual ROI segmentation because of potential image discontinuities between subareas.

Action potential analysis

For analysis and detection of spiking-related voltage signals, slow fluctuations in fluorescence signals for each cell were first removed by baseline subtraction along a moving average across 2.5 s of recordings. Given the rise and decay time of tested GEVIs, a putative spike trace was generated by calculating the difference in fluorescence intensity across every tenth imaging frame (12.5 ms) across the time series. The putative spike trace was normalized by the cell's noise level, defined as the mean of the absolute difference between each time point to produce an SNR trace. Spikes were identified as transient events exceeding a given SNR threshold. Sensory-evoked action potentials were identified as detected spikes occurring within a 20-frame window (25 ms) following air puff delivery. The sensitivity of GEVIs for spike detection was assessed by quantifying the percentage of detected action potentials evoked for each air puff across a range of SNR thresholds.

Photobleaching

Photobleaching measurements were performed using the SMURF two-photon microscope on male and female adult (6- to 8-week-old, 11 total) C57BL/6 mice with implanted cranial windows. Imaging was performed using a total laser power of 240 mW at the sample (30 mW per beam). The tissue was scanned at a frame rate of 803 Hz. An intermittent scanning pattern was used, consisting of 9 s on (shutter open) and 4 s off (shutter closed) for 60 min. Continuous scanning was performed with laser shutter at 59 s on and 1 s off (to allow for saving of image data) for 60 min. To assess action potential responses during photobleaching, voltage imaging with whisker stimulation was performed at 15-min intervals. ROIs corresponding to a single cell were extracted manually. Each data point corresponded to the mean fluorescence intensity of every 20th frame across one session of imaging (9 s in intermittent condition, and 59 s in continuous condition). Photobleaching rates were determined by normalizing all data points to the first data point.

Thermal measurements

Animals were prepared using the same procedure as for in vivo electrophysiology. Four male and female adult (6- to 8-week-old) C57BL/6 mice were anesthetized with 1.5% isoflurane and head-fixed under the SMURF two-photon microscope with a heating pad underneath. An ultrafine flexible microprobe (IT-24P, Physitemp Instuments) connected to a thermometer (TH-5, Physitemp Instuments) was placed on brain surface immediately adjacent to the imaging area. Two-photon multibeam excitation (eight beams, 30 mW per beam) was performed at 100-μm depth below the pial surface, scanning a 400 μm × 400 μm area at 803 Hz continuously over 1 h. Temperature readings were recorded regularly every 15–60 s.

Brain motion simulation

Two-dimensional rigid frame motion was applied to the raw in vivo image time series of SpikeyGi-expressing neurons acquired with the SMURF two-photon microscope. Simulated motion was based on a maximum tissue velocity of 0.32 μm ms^{-1} and a maximum total displacement of 5.7 μm based on previously reported measurements[26]. Assuming an x/y resolution of 1.0/2.1 μm per pixel and frame rate of 803 Hz, motion vectors

describing frame-to-frame subpixel shifts (dx or dy) were generated by random sampling from a Gaussian distribution with x/y mean of 0/0 pixels, s.d. of 0.175/0.0875, and threshold between ±0.4 and ±0.2 pixels. A displacement vector (Dx or Dy) was calculated by integrating across the motion vector. Displacement vectors with different degrees of maximum total displacement (low, D_{max} x/y = ±2/±1 pixels; medium, D_{max} x/y = ±4/±2 pixels; high, D_{max} x/y = ±6/±3 pixels) were constructed by reversing the sign of the motion vector when Dx or Dy reached D_{max}. Subpixel displacement vectors were rounded to the nearest pixel values and then applied to the raw in vivo image time series. The image time series was then denoised by the trained DeepVID model.

Photodamage

Animals previously injected with virus and implanted with cranial windows were used for experiments. This consisted of male and female adult (6- to 8-week-old, 4 total) C57Bl/6 mice. A location for laser exposure away from the viral injection sites was selected based on a wide-field blood vessel map under the cranial window. Each photodamage session consisted of 1 h of continuous laser scanning with 240-mW total power (30-mW per beamlet). Sixteen hours after laser exposure, animals were anesthetized with 1.5%–3.0% isoflurane, and cranial windows were removed to expose the cortex. The blood vessel map was used to locate the laser exposure site, and a lipophilic dye (SP-DiIC$_{18}$(3); ThermoFisher Scientific; D7777) was injected to mark the four corners of the laser exposure field of view. Animals were then transcardially perfused with 0.1 M PBS and 4% paraformaldehyde. Brains were postfixed in 4% paraformaldehyde for 24 h, transferred to 0.1 M PBS, and sliced with a vibratome into 50-μm coronal sections. Slices were first incubated in a blocking solution (10% normal goat serum and 1% Triton X-100) and washed three times in 0.1 M PBS. Alternating slices were labeled with sets of primary antibodies in 5% normal goat serum and 0.1% Triton X-100. One set of slices was stained with primary antibodies for mouse monoclonal anti-GFAP (G3893, Sigma-Aldrich; 1:1,000 dilution) and rabbit anti-Iba1 (019–19741, Wako Chemicals; 1:500 dilution). The other set of slices was stained with mouse anti-HSP70/HSP72 (ADI-SPA-810-D; Enzo Life Sciences; 1:400 dilution), and rabbit anticleaved caspase-3 (Asp175) (no. 9661, Cell Signaling; 1:250 dilution). Slices were then washed three times in 0.1 M PBS and incubated in secondary antibodies. Iba1 and caspase-3 were labeled with goat anti-rabbit Alexa Fluor 555 (A21429, Invitrogen; 1:500 dilution), and GFAP and HSP were labeled with goat anti-mouse Alexa Fluor 647 (A21235, Invitrogen; 1:500 dilution). Slices were washed in 0.1 M PBS and mounted with Fluoromount-G mounting medium (0100–01, SouthernBiotech). The lipophilic dye was used to identify which sections contained the laser exposure site and where it was located on the medial–lateral axis. Slices were imaged with a Nikon ECLIPSE Ni-E microscope and NIS-Elements software (Nikon Instruments).

Photodamage was determined by increased antibody labeling in the laser-exposed region relative to the corresponding area on the contralateral hemisphere. The relative fluorescence was determined by dividing the mean fluorescent intensity on the treated hemisphere by the mean intensity on the contralateral hemisphere. Fluorescence was measured in two areas of the cortex: the laser exposure site and a control area that was at least 1 mm away from the site of laser exposure. The control area was intended to capture protein expression that may

have been caused by chronic window implantation and/or virus injection but was not caused by laser exposure.

Reporting summary

Further information on research design is available in the Nature Portfolio Reporting Summary linked to this article.
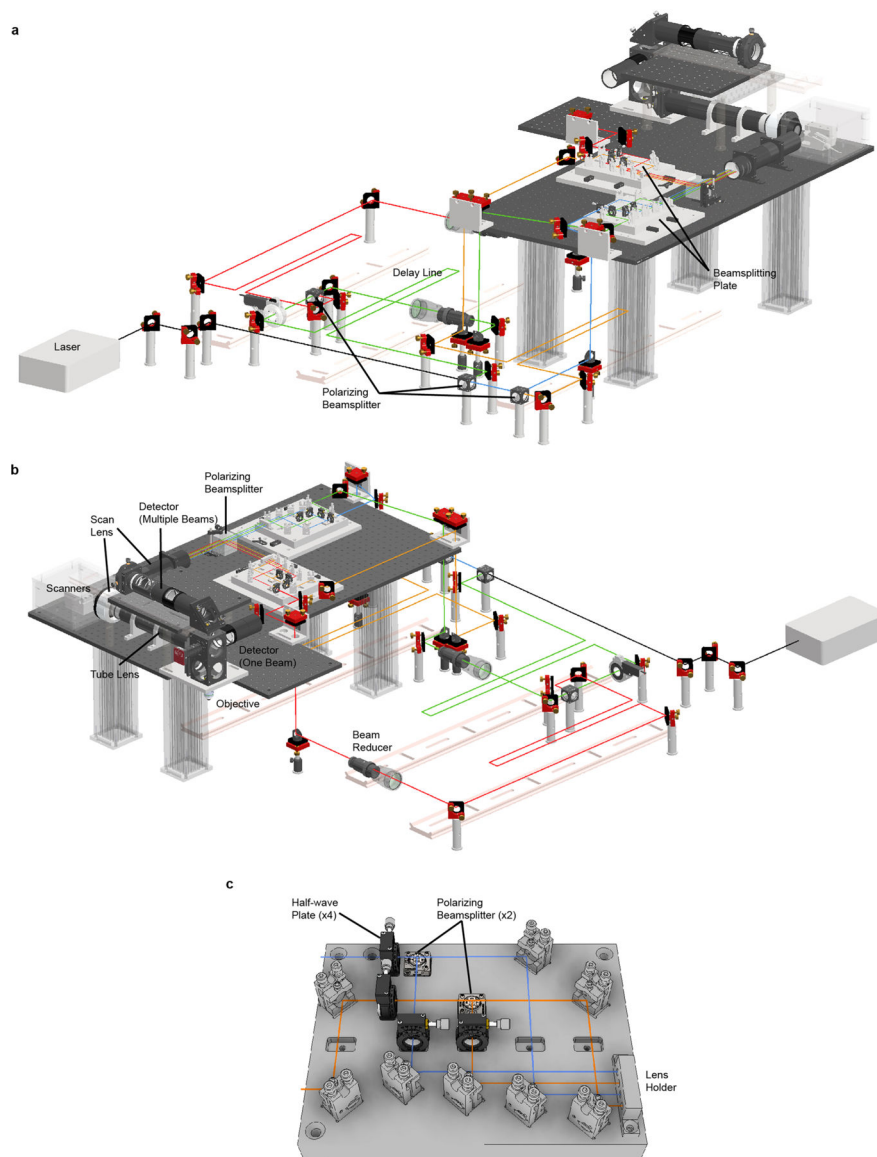
Extended Data
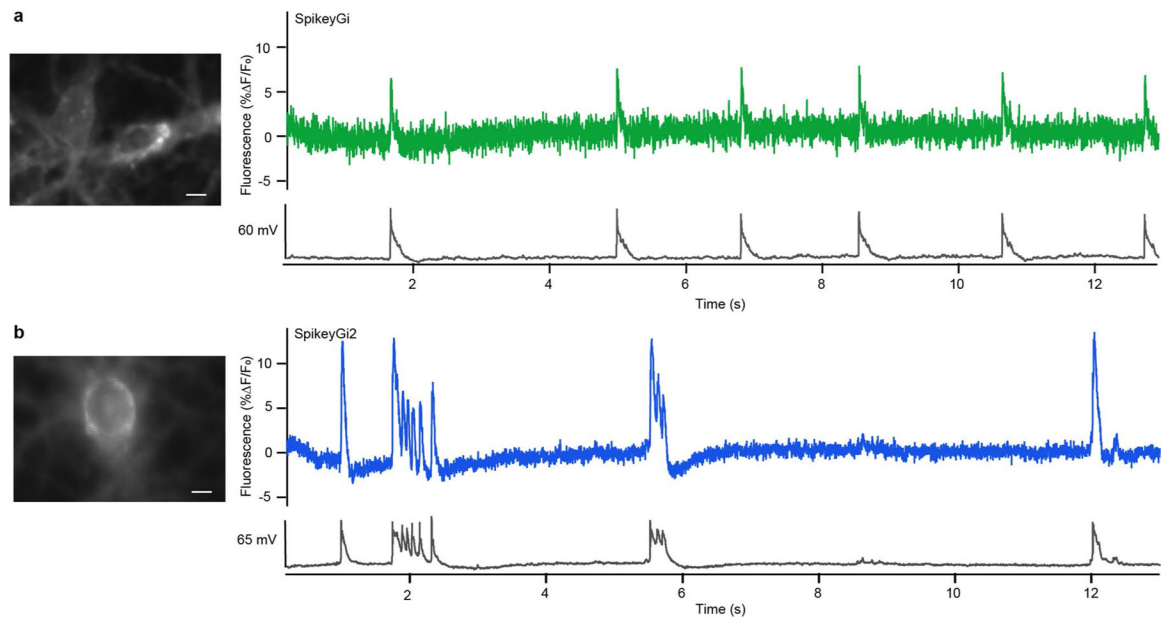
Extended Data Fig. 1 |. Single-photon imaging of spontaneous activity in cultured mouse neurons expressing SpikeyGi or SpikeyGi2.
(a) Single-photon image of a SpikeyGi-expressing neuron (left). Fluorescence response to spontaneous neuronal activity imaged at 500 Hz (right). This experiment was performed 3 times with similar results. **(b)** Single-photon image of a SpikeyGi2-expressing neuron (left). Fluorescence response to spontaneous neuronal activity imaged at 500 Hz (right). This experiment was performed 5 times with similar results. Similar signals were recorded in three SpikeyGi and five SpikeyGi2 neurons. Scale bar: 5 μm.
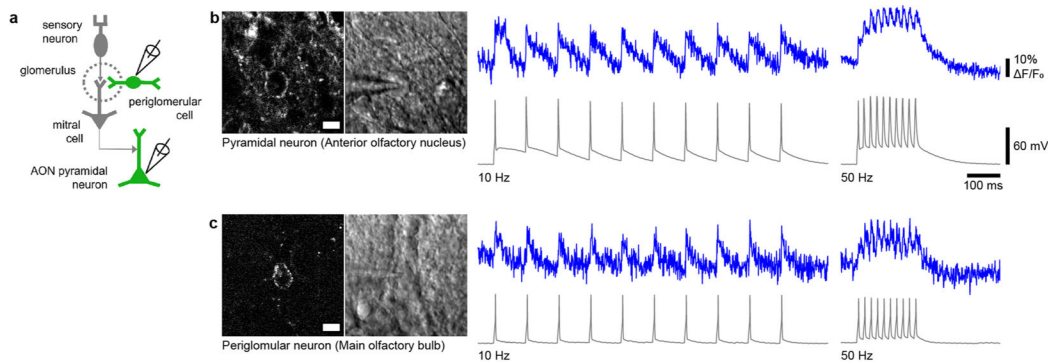
Extended Data Fig. 2 |. SpikeyGi2 responses *in vitro* across neuronal cell types.
(a) Circuit diagram of recorded cell types in the anterior olfactory nucleus and main olfactory bulb. **(b)** Example of *in vitro* fluorescence in an anterior olfactory nucleus pyramidal neuron expressing SpikeyGi2 in response to 10 Hz and 50 Hz action potential trains. **(c)** Example of *in vitro* fluorescence in a main olfactory bulb periglomular neuron expressing SpikeyGi2 in response to10 Hz and 50 Hz action potential trains. Scale bar: 10 μm. These experiments were performed 5 times with similar results.

Extended Data Fig. 3 |. Opto-mechanical design of SMURF 2P microscope.
(a, **b)** CAD design rendering of our fast microscope. **(c)** CAD design rendering of the beam splitter plate.
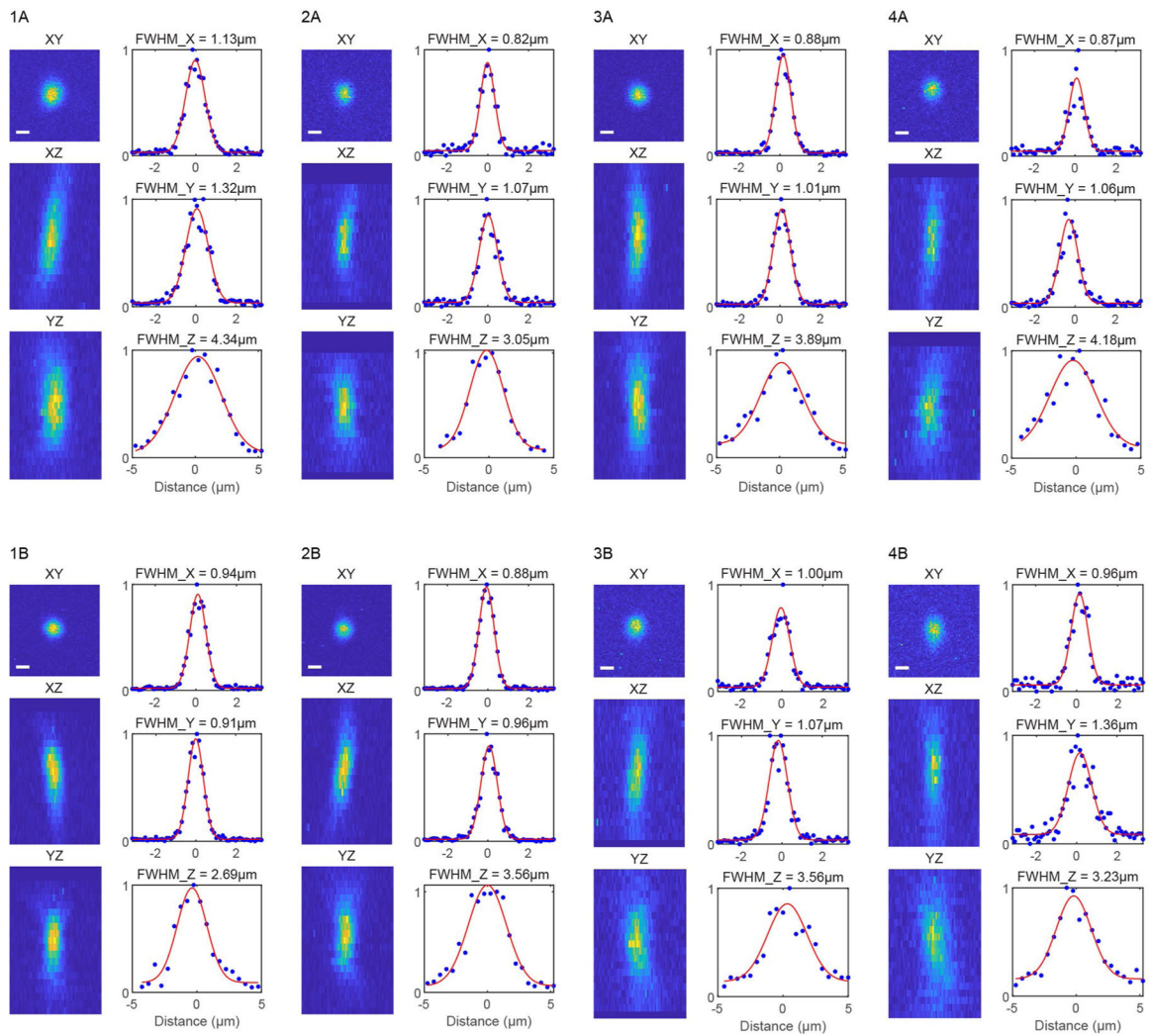
Extended Data Fig. 4 |. Example point spread function measurements for each beamlet in the SMURF 2P microscope.

Scale bar: 1 μm. Examples are shown from $n = 7$ beads, 1A; 10 beads, 2A; 10 beads, 3A; 10 beads, 4A; 11 beads, 1B; 9 beads, 2B; 10 beads, 3B; 10 beads, 4B.
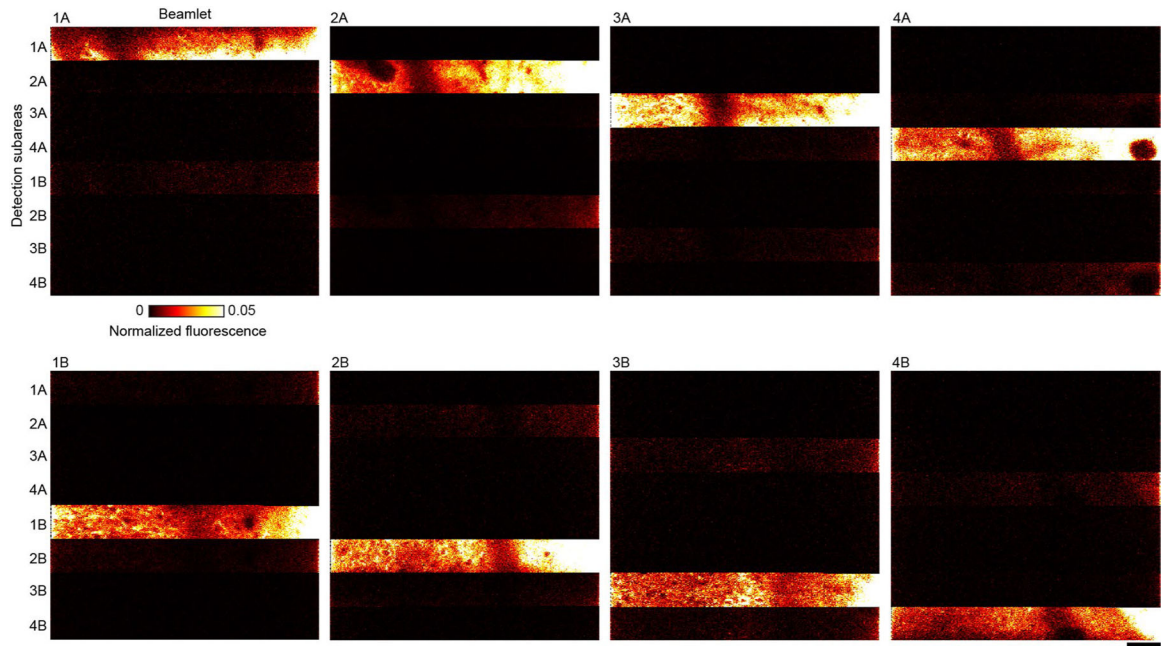
Extended Data Fig. 5 |. Detected Crosstalk *In Vivo*.
Example of crosstalk from each beamlet observed across each detected subarea. *In vivo* images are of SpikeyGi expression at ~150 μm below the pial surface. Scale bar: 50 μm.
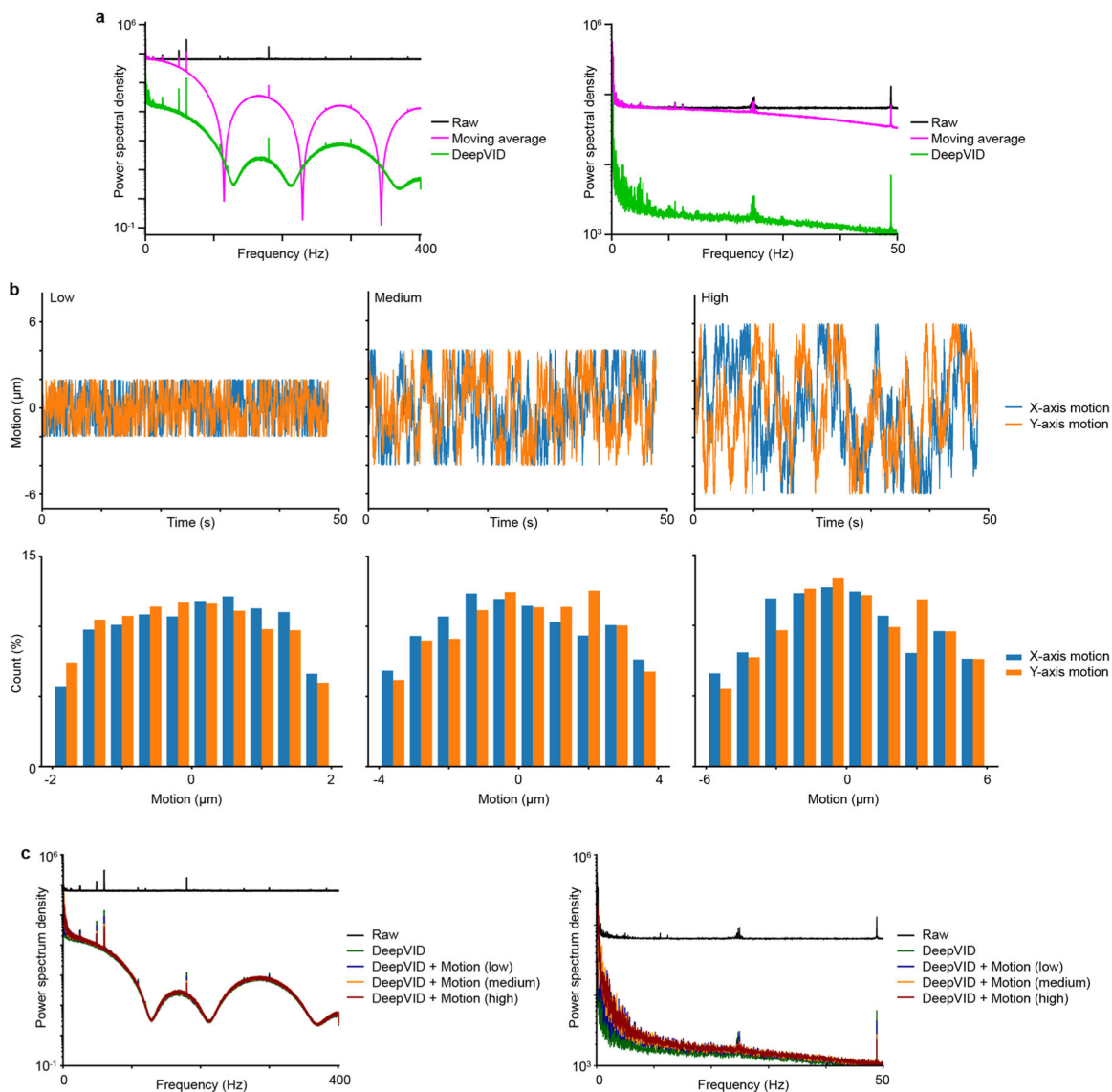
Extended Data Fig. 6 |. Analysis of DeepVID performance.
(a) Power spectrum analysis comparing DeepVID denoising against raw and 7-frame moving average for all frequencies (left) and 0–50 Hz (right). **(b)** Top panels show simulated motion traces in X- and Y-axis at three levels of residual motion artifacts corresponding to a maximum total displacement at (low) ±2, (medium) ±4, and (high) ±6 µm. **(c)** Power spectrum analysis of DeepVID denoising results at different motion artifact levels for all frequencies (left) and 0–50 Hz (right).
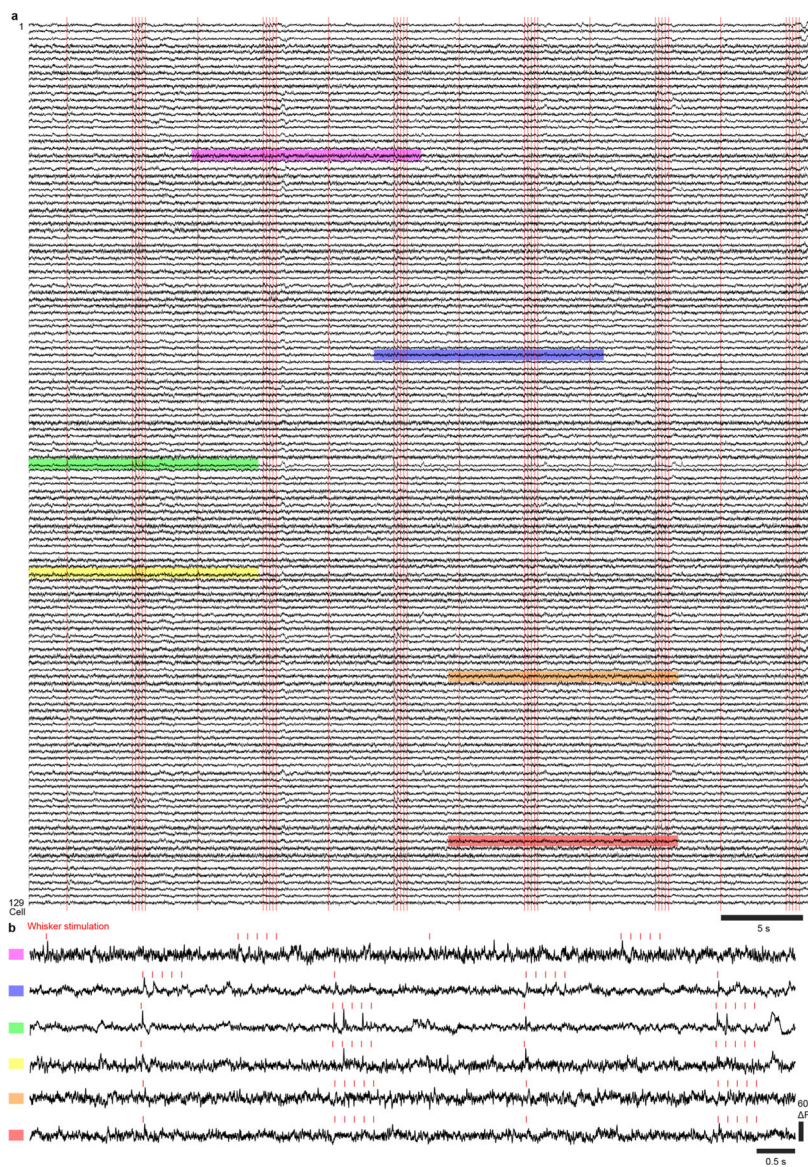
Extended Data Fig. 7 |. *In vivo* **population imaging of SpikeyGi from SMURF 2P microscope.**
(a) Fluorescence traces from simultaneous recordings across 129 S1 neurons from our fast microscope acquired at 803 Hz. Raw images were denoised with DeepVID. For visualization purposes, traces are detrended with 2.5 sec moving average and low pass filtered at 200 Hz. Red lines indicate air puff whisker stimulus. Detected action potentials are plotted in Fig. 5b. **(b)** Magnified view of example traces across different cells. Squares denote traces corresponding to shaded regions of the same color indicated in [a]. Red lines indicate air puff whisker stimulus.
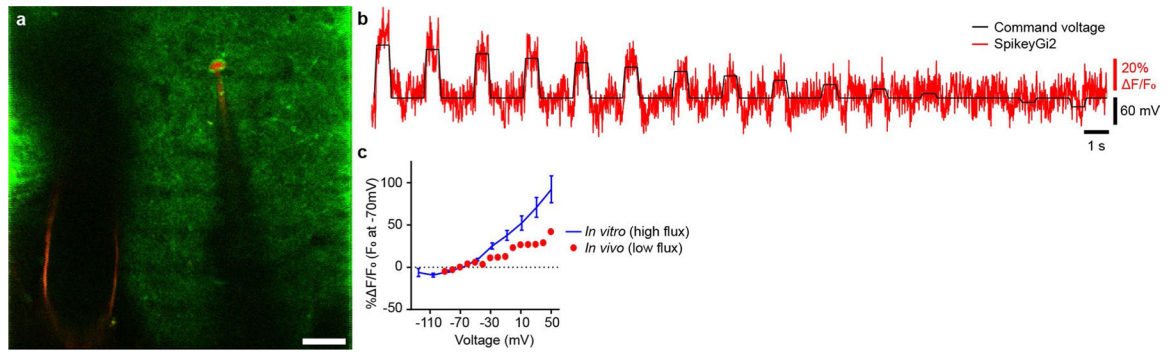
Extended Data Fig. 8 |. *In vivo* patch recording in SpikeyGi2 expressing neuron.
(a) *In vivo* two-photon image of targeted S1 neuron (red) expressing SpikeyGi2 (green). Scale bar: 50 μm. This experiment was performance once. **(b)** Fluorescence response to applied voltage steps. **(c)** Measured fluorescence response from example neuron overlaid with fluorescence responses measured *in vitro* (*in vitro*, $n = 6$ cells; 10 trials per step). Error bars; S.E.M.
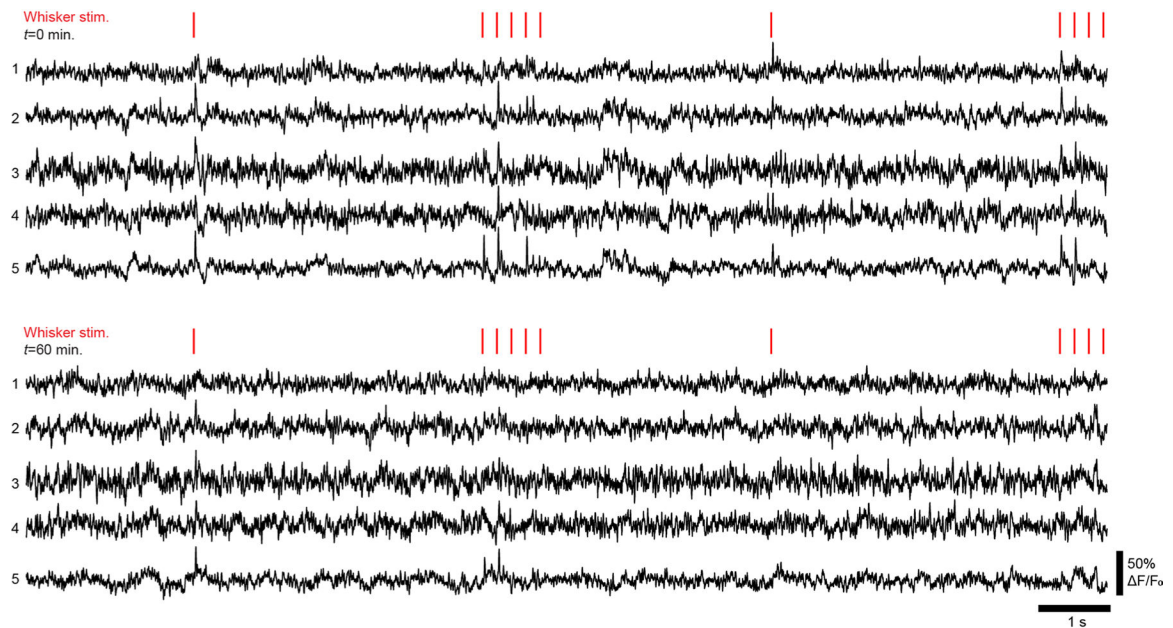
Extended Data Fig. 9 |. Example SpikeyGi fluorescence traces from 5 neurons across 1 hour of *in vivo* imaging.

Supplementary Material

Refer to Web version on PubMed Central for supplementary material.

Acknowledgements

Data availability

The DNA sequences are available in GenBank under accession numbers OQ143892 (SpikeyGi) and OQ143893 (SpikeyGi2). The plasmid pAAV-hSyn-SpikeyGi2-kv2.1 (no. 82031) is available through Addgene. Experimental data are available at https://doi.org/10.12751/g-node.1b9v1w.

References

1. & Huang L et al. Relationship between simultaneously recorded spiking activity and fluorescence signal in GCaMP6 transgenic mice.eLife 10, e51675 (2021). [PubMed: 33683198]

2. Wilt BA, Fitzgerald JE & Schnitzer MJ Photon shot noise limits on optical detection of neuronal spikes and estimation of spike timing. Biophys. J 104, 51–62 (2013). [PubMed: 23332058]

3. Sjulson L & Miesenbock G Optical recording of action potentials and other discrete physiological events: a perspective from signal detection theory. Physiology 22, 47–55 (2007). [PubMed: 17289930]

4. Abdelfattah AS et al. Bright and photostable chemigenetic indicators for extended in vivo voltage imaging. Science 365, 699–704 (2019). [PubMed: 31371562]

5. Villette V et al. Ultrafast two-photon imaging of a high-gain voltage indicator in awake behaving mice. Cell 179, 1590–1608. e1523 (2019). [PubMed: 31835034]

6. Wu J et al. Kilohertz two-photon fluorescence microscopy imaging of neural activity in vivo. Nat. Methods 17, 287–290 (2020). [PubMed: 32123392]

7. Piatkevich KD et al. Population imaging of neural activity in awake behaving mice. Nature 574, 413–417 (2019). [PubMed: 31597963]

8. Adam Y et al. Voltage imaging and optogenetics reveal behaviour-dependent changes in hippocampal dynamics. Nature 569, 413–417 (2019). [PubMed: 31043747]

9. Zhang T et al. Kilohertz two-photon brain imaging in awake mice. Nat. Methods 16, 1119–1122 (2019). [PubMed: 31659327]

10. Chamberland S et al. Fast two-photon imaging of subcellular voltage dynamics in neuronal tissue with genetically encoded indicators. eLife 6, e25690 (2017). [PubMed: 28749338]

11. Jin L et al. Single action potentials and subthreshold electrical events imaged in neurons with a fluorescent protein voltage probe. Neuron 75, 779–785 (2012). [PubMed: 22958819]

12. Abdelfattah AS et al. A general approach to engineer positive-going eFRET voltage indicators. Nat. Commun 11, 3444 (2020). [PubMed: 32651384]

13. Podgorski K & Ranganathan G Brain heating induced by near-infrared lasers during multiphoton microscopy. J. Neurophysiol 116, 1012–1023 (2016). [PubMed: 27281749]

14. Platisa J, Vasan G, Yang A & Pieribone VA Directed evolution of key residues in fluorescent protein inverses the polarity of voltage sensitivity in the genetically encoded indicator arclight. ACS Chem. Neurosci 8, 513–523 (2017). [PubMed: 28045247]

15. Xu F, Shi DQ, Lau PM, Lin MZ & Bi GQ Excitation wavelength optimization improves photostability of ASAP-family GEVIs. Mol. Brain 11, 32 (2018). [PubMed: 29866136]

16. Bando Y, Sakamoto M, Kim S, Ayzenshtat I & Yuste R Comparative evaluation of genetically encoded voltage indicators. Cell Rep 26, 802–813 e804 (2019). [PubMed: 30650368]

17. Chen JL, Voigt FF, Javadzadeh M, Krueppel R & Helmchen F Long-Range population dynamics of anatomically defined neocortical networks. eLife 5, e14679 (2016). [PubMed: 27218452]

18. Cheng A, Goncalves JT, Golshani P, Arisaka K & Portera-Cailliau C Simultaneous two-photon calcium imaging at different depths with spatiotemporal multiplexing. Nat. Methods 8, 139–142 (2011). [PubMed: 21217749]

19. Amir W et al. Simultaneous imaging of multiple focal planes using a two-photon scanning microscope. Opt. Lett 32, 1731–1733 (2007). [PubMed: 17572762]

20. Clough M et al. Flexible simultaneous mesoscale two-photon imaging of neural activity at high speeds. Nat. Commun 12, 6638 (2021). [PubMed: 34789730]

21. Kim KH et al. Multifocal multiphoton microscopy based on multianode photomultiplier tubes. Opt. Express 15, 11658–11678 (2007). [PubMed: 19547526]

22. Charan K, Li B, Wang M, Lin CP & Xu C Fiber-based tunable repetition rate source for deep tissue two-photon fluorescence microscopy. Biomed. Opt. Express 9, 2304–2311 (2018). [PubMed: 29760989]

23. Lecoq J et al. Removing independent noise in systems neuroscience data using DeepInterpolation. Nat. Methods 18, 1401–1408 (2021). [PubMed: 34650233]

24. Li X et al. Reinforcing neuron extraction and spike inference in calcium imaging using deep self-supervised denoising. Nat. Methods 18, 1395–1400 (2021). [PubMed: 34400836]

25. Krull A, Buchholz T & Jug F Noise2Void - Learning Denoising From Single Noisy Images. In 2019 IEEE/CVF Conference on Computer Vision and Pattern Recognition (CVPR) 2124–2132 (IEEE, 2019).

26. Griffiths VA et al. Real-time 3D movement correction for two-photon imaging in behaving animals. Nat. Methods 17, 741–748 (2020). [PubMed: 32483335]

27. & Feldmeyer D et al. Barrel cortex function.Prog. Neurobiol 103, 3–27 (2013). [PubMed: 23195880]

28. Yamashita T et al. Membrane potential dynamics of neocortical projection neurons driving target-specific signals. Neuron 80, 1477–1490 (2013). [PubMed: 24360548]

29. Demas J et al. High-speed, cortex-wide volumetric recording of neuroactivity at cellular resolution using light beads microscopy. Nat. Methods 18, 1103–1111 (2021). [PubMed: 34462592]

30. Weisenburger S et al. Volumetric Ca^{2+} imaging in the mouse brain using hybrid multiplexed sculpted light microscopy. Cell 177, 1050–1066.e1014 (2019). [PubMed: 30982596]

31. Vaswani A et al. Attention is all you need. In Advances in Neural Information Processing Systems 30 (Eds Guyon I et al.) 5998–6008 (NIPS, 2017).

32. Challis RC et al. Systemic AAV vectors for widespread and targeted gene delivery in rodents. Nat. Protoc 14, 379–414 (2019). [PubMed: 30626963]

33. Platisa J, Han Z & Pieribone VA Different categories of fluorescent proteins result in GEVIs with similar characteristics. Preprint at bioRxiv 10.1101/2020.05.06.081018 (2020).

34. Park J et al. Screening fluorescent voltage indicators with spontaneously spiking HEK cells. PLoS ONE 8, e85221 (2014).

35. Zhang K, Zuo W, Chen Y, Meng D & Zhang L Beyond a Gaussian denoiser: residual learning of deep CNN for image denoising. IEEE Trans. Image Process 26, 3142–3155 (2017). [PubMed: 28166495]
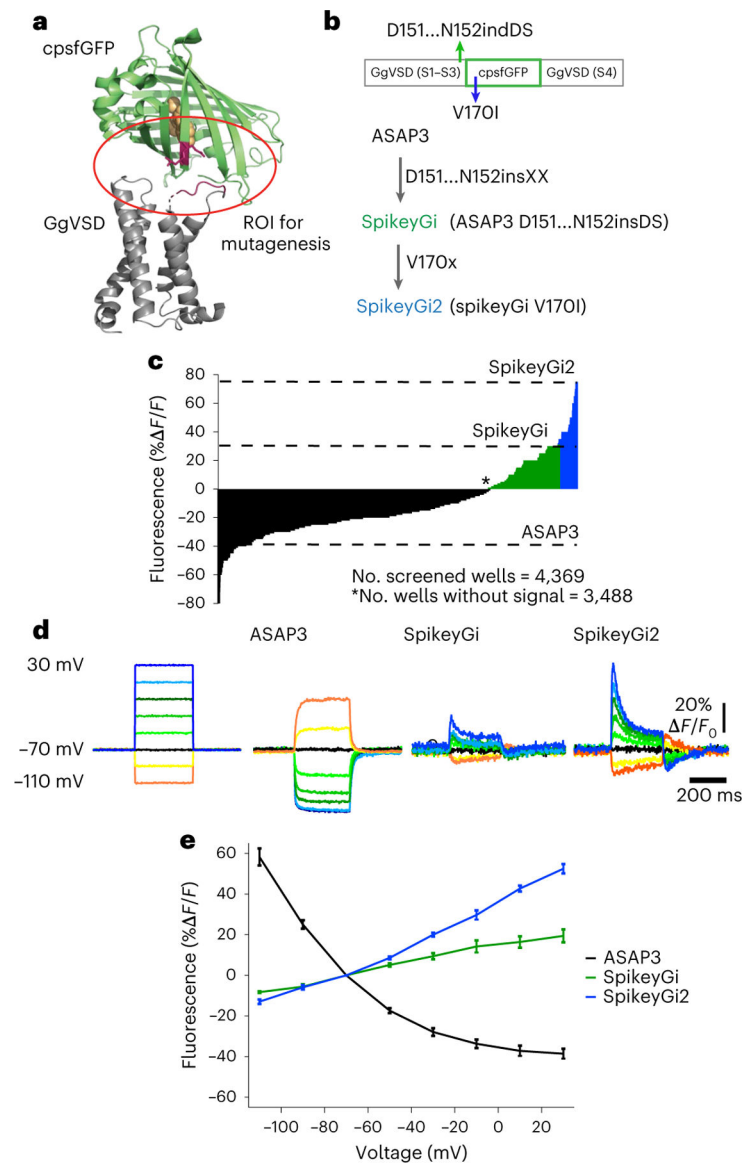
Fig. 1 |. Design and functional characterization of green, positive-going, two-photon-compatible GEVIs.

a, A model of the crystal structure for SpikeyGi and SpikeyGi2 based on crystal structures for cpEGFP (PDB 3EVP) and CiVSD (PDB 4G7Y). The ROI for targeted mutagenesis is labeled (red circle). **b**, Top, a topographic scheme of ASAP3 showing amino acid insertions (DS) between residues D151 and N152 that produced SpikeyGi (green arrow), and single point mutation V170I within cpGFP that produced SpikeyGi2 (blue arrow). All amino acid numbering is based on the starting Met in ASAP3. Bottom, schematic of directed evolution of GEVIs. **c**, Distribution of fluorescence responses of ASAP3 mutants expressed in electrically active HEK293 cells in response to field stimulation. ASAP3 was used in the first evolution round and produced positive-going mutants shown in green. SpikeyGi was used in the second evolution round and produced mutants shown in blue. **d**, Example traces showing fluorescence response to a series of voltage steps recorded from HEK293 cells expressing ASAP3, SpikeyGi, and SpikeyGi2. **e**, Fluorescence response of indicators across

a range of voltage steps. For all cells, 300-ms voltage steps of −40 to +100 mV were applied in increments of 20 mV from a resting potential of −70 mV. (ASAP3, $n = 5$ cells; SpikeyGi, $n = 3$ cells; SpikeyGi2, $n = 6$ cells). Error bars, s.e.m.
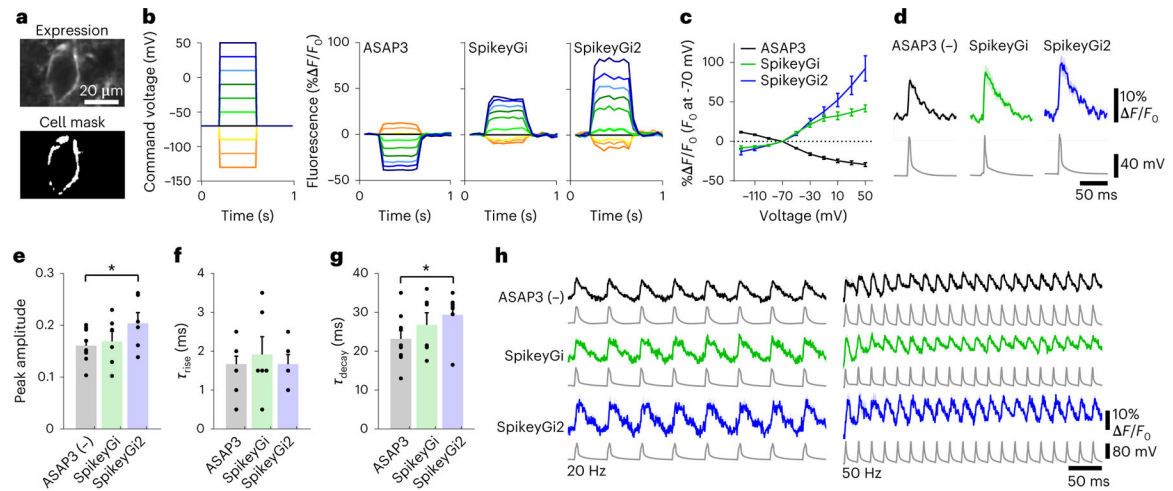
Fig. 2 |. In vitro performance of SpikeyGi and SpikeyGi2.

a, Example of S1 neuron expressing SpikeyGi imaged in brain slice (top). ROI mask used for image analysis (bottom). This experiment was repeated 25 times independently with similar results. **b**, Example command voltage steps applied during voltage-clamp recordings (left). Corresponding fluorescence responses measured in example ASAP3, SpikeyGi and SpikeyGi2 cells. **c**, Fluorescence responses to steady-state voltage steps in slice electrophysiology for individual S1 cells (normalized to −70 mV). **d**, Fluorescence responses to single action potentials evoked by current injection in vitro. **e**, Peak amplitude (amp.) to a single action potential. **f**, Rise time to a single action potential. **g**, Decay time to a single action potential. **h**, Average fluorescence responses to 20-Hz and 50-Hz trains of action potentials. Shaded region, s.e.m. Error bars, s.e.m. *$P < 0.05$; Student's t-test. $n = 8$ cells from five animals, ASAP3; $n = 8$ cells from eight animals, SpikeyGi; $n = 9$ cells from seven animals, SpikeyGi2; 10 trials per step **c**. $n = 9$ cells from six animals, ASAP3; $n = 6$ cells from four animals, SpikeyGi; $n = 6$ cells from five animals, SpikeyGi2; 10 trials per steps **d**–**g**.
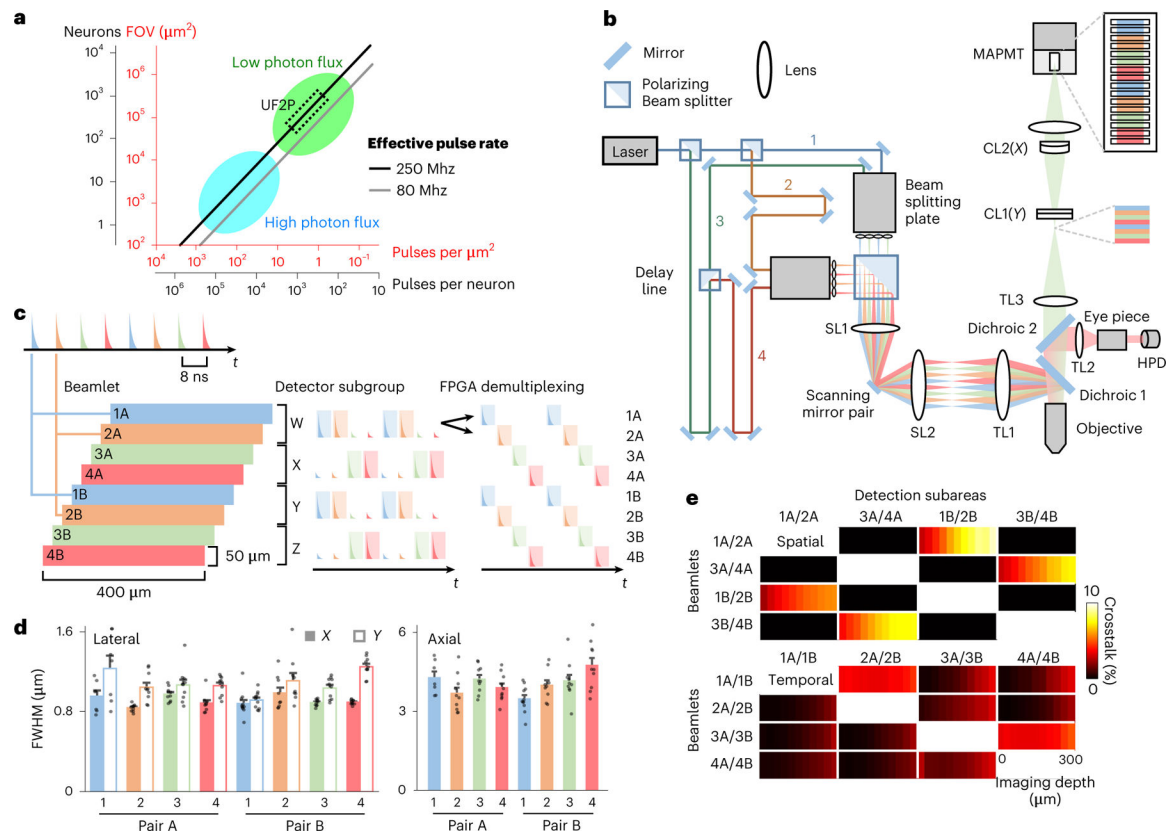
Fig. 3 |. Design and performance of SMURF two-photon microscope.
a, Relationship between excitation pulses per neuron and total neurons imaged at a 1-kHz sampling rate assuming 1-μm^2 voxels across different effective pulse rates. **b**, Schematic of the SMURF two-photon microscope. The laser beam was first split into four beamlets (blue, 1; orange, 2; green, 3; red, 4) using polarizing beam splitters (PBSs). Beamlets were temporally multiplexed using delay lines and then split into spatially multiplexed beamlet pairs. Using two beam splitting plates, beamlets were spatially arranged, combined with a 2-inch PBS into a linear arrangement, and projected onto the objective back pupil. Scan lenses (SL) and tube lenses (TL) were matched to the beam diameter between the resonant–galvo scanner pair and the size of the objective back aperture. The detection path enabled single-color imaging with all eight beamlets or dual-color imaging with a single beam. A dichroic separated green from red fluorescence. Red fluorescence excited from a single beam was detected with a single hybrid PMT. For green fluorescence, cylindrical lenses (CL) in the detection path reshaped the collected fluorescence to match a linearly arranged 16 × 1 MAPMT detector. Signals from each anode were independently collected when imaging using eight beamlets or summed when excited with a single beam. **c**, Schematic of detection and demultiplexing algorithm. Left panel shows arrangement of the imaged subareas at the sample. The 16 anodes on the MAPMT were summed into four detector subgroups (W, X, Y and Z). Each detector subgroup received photons from two temporally multiplexed subareas that were subsequently demultiplexed using FPGA programmed digital gates (shaded area). Additional time-dependent gating was implemented on the FPGA to minimize spatial multiplexed crosstalk from neighboring detector subgroups. **d**, Lateral and

axial point spread function measurements for each beamlet ($n = 7$ beads, 1A; 10 beads, 2A; 10 beads, 3A; 10 beads, 4A; 11 beads, 1B; 9 beads, 2B; 10 beads, 3B; 10 beads, 4B). Error bar, s.e.m. **e**, Average detected crosstalk as a function of imaging depth because of spatial multiplexing (top) or temporal multiplexing (bottom). $n = 5$ imaging stacks.
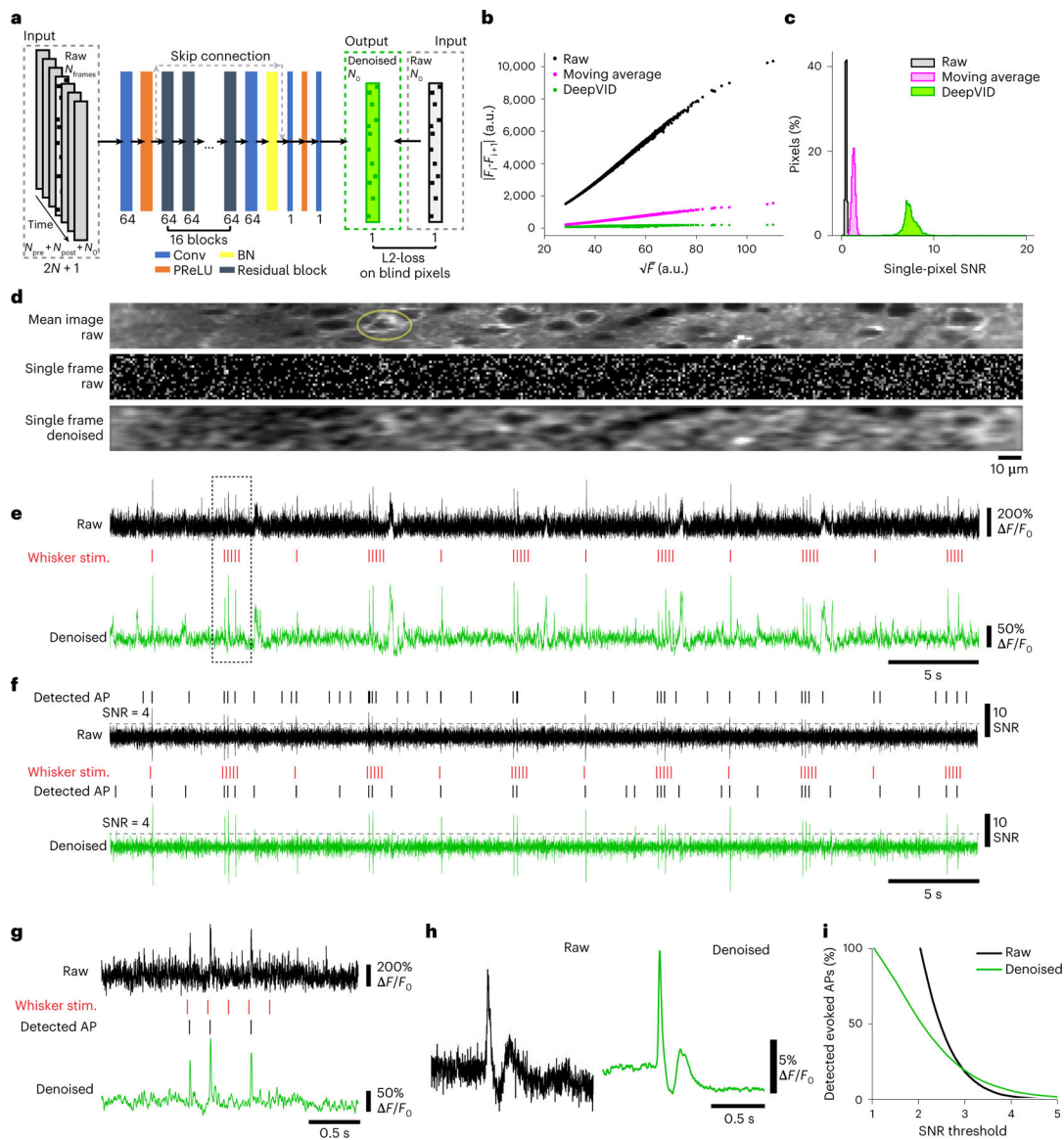
Fig. 4 |. DeepVID reduces photon shot noise to improve action potential detection.
a, Training strategy and network structure of DeepVID. The voltage signals from blind-spot pixels in the central frame (N_0) are inferred from the rest of unmasked pixels in the central frame and the neighboring frames (N_{pre} and N_{post}) in the input image data. DeepVID is a deep convolutional neural network with residual blocks, where Conv is 2D convolution, BN is batch normalization, and PReLU is the parametric rectified linear unit. **b**, Frame-to-frame noise (mean of the absolute intensity difference) as a function of fluorescence signal (square root of the mean intensity) for raw pixels, denoised pixels by seven-frame moving average, and denoised pixels by DeepVID for representative image data. a.u., arbitrary units. **c**, Distribution of pixel-level SNR (temporal mean over s.d. for each pixel time series) from representative raw data, denoised data by seven-frame moving average, and denoised data by DeepVID. **d**, Example of single-frame image denoising with DeepVID. Images from one subarea acquired with our microscope. Raw in vivo image averaged across 1,000

frames (top) showing SpikeyGi-expressing neurons. Single frame is shown before (middle) and after denoising with DeepVID (bottom). This experiment was performed 50 times independently with similar results. **e**, Raw and denoised fluorescence traces from neuron (circled in **d**). Air puff whisker stimuli are shown. stim., stimulation. **f**, Putative spike events based on SNR levels in raw and denoised traces. Detected events at SNR > 4 are shown. **g**, High temporal resolution view of example raw and denoised traces (box in **e**) showing spike-related fluorescence changes. **h**, Average raw and denoised fluorescence traces in response to single air puff stimulus. **i,** In vivo detection of sensory-evoked action potentials with SpikeyGi across SNR thresholds for raw and denoised traces ($n = 214$ cells, three animals). Shaded region, s.e.m.
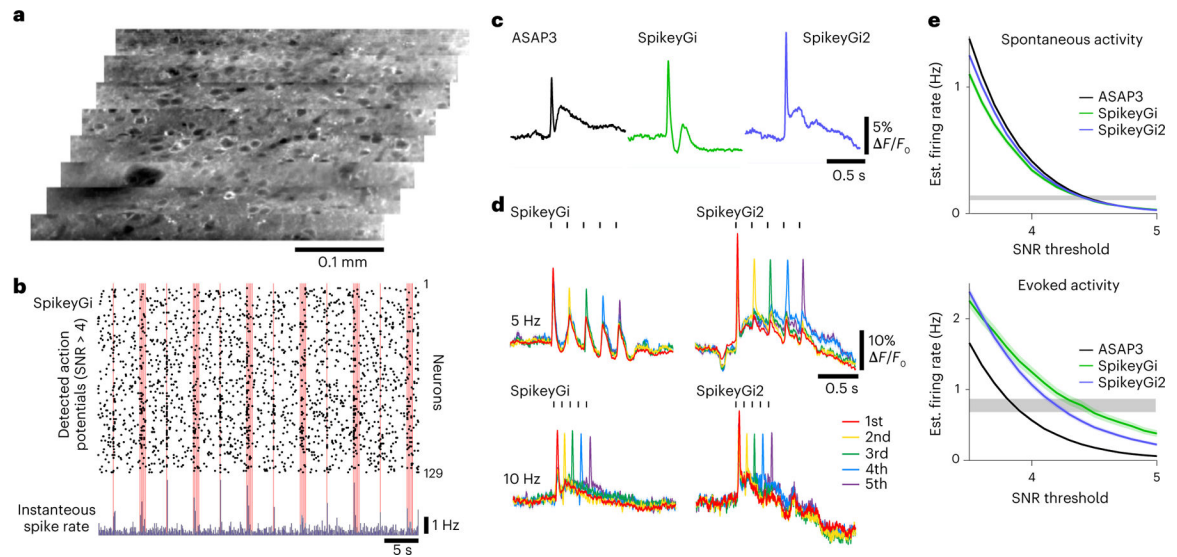
Fig. 5 |. SpikeyGi and SpikeyGi2 performance during in vivo two-photon population imaging.
a, Example FOV from our microscope of layer 2/3 S1 neurons expressing SpikeyGi. This experiment was performed 50 times independently with similar results. **b**, Detected in vivo spike trains at SNR > 4 for 129 simultaneously imaged neurons expressing SpikeyGi. Red lines indicate air puffs. Instantaneous spike rate across the population is shown at the bottom. **c**, Average denoised fluorescence traces in response to single air puff stimulus for ASAP3, SpikeyGi and SpikeyGi2 (for ASAP3, $n = 1,012$ cells, two animals; for SpikeyGi, $n = 214$ cells, three animals; for SpikeyGi2, $n = 311$ cells, two animals). **d**, Average fluorescence responses for SpikeyGi and SpikeyGi2 to 5-Hz or 10-Hz stimulus trains. Each color trace corresponds to the average response to all detected action potentials (SNR > 4) associated with individual air puffs within the train (for SpikeyGi, 5-Hz stimuli, $n = 214$ cells, three animals; for SpikeyGi, 10-Hz stimuli, $n = 206$ cells, three animals; for SpikeyGi2, 5-Hz stimuli, $n = 311$ cells, two animals; for SpikeyGi2, 10-Hz stimuli, $n = 201$ cells, two animals). **e**, Estimated (Est.) spontaneous and evoked firing rates for detected action potentials across SNR thresholds for ASAP3, SpikeyGi and SpikeyGi2. Shaded region, s.e.m.
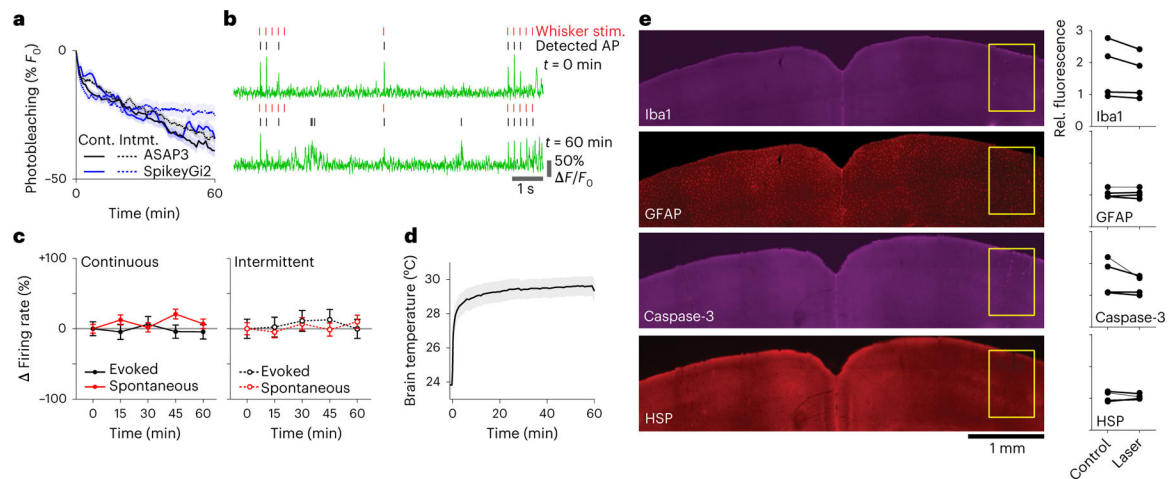
Fig. 6 |. Low-photon flux excitation facilitates sustained two-photon voltage imaging.
a, In vivo photobleaching curves for ASAP3 and SpikeyGi2 during near continuous (cont.; 59 s on, 1 s off) or intermittent imaging (intmt.; 9 s on, 4 s off) in S1 under low-photon flux conditions (continuous for ASAP3, $n = 44$ cells, four FOV, two animals; continuous for SpikeyGi2, $n = 46$ cells, five FOV, four animals; intermittent for ASAP3, $n = 52$ cells, four FOV, three animals; continuous for SpikeyGi2, $n = 45$ cells, four FOV, two animals). **b**, Example SpikeyGi fluorescence traces and detected action potentials (SNR > 4) of a neuron across 1 h of intermittent in vivo imaging. **c**, Relative change in spontaneous and evoked firing rates for detected action potentials (SNR > 4) across 1 h of continuous imaging ($n = 125$ cells, one animal) or intermittent imaging ($n = 71$ cells, one animal). **d**, Surface brain temperature across 1 h of continuous imaging using the SMURF two-photon microscope ($n = 4$ animals). **e**, Left panels show example coronal sections of immunostained tissue assaying photodamage after 1 h of continuous imaging. Yellow box denotes imaged region. Right panels show relative (Rel.) fluorescence in imaged region compared with the corresponding contralateral region areas across immunostained tissue ($n = 4$ animals). This experiment was performed four times independently with similar results. Scale bar, 1 mm. Shaded region (**a**, **d**), s.e.m. Error bars (**c**), s.e.m.